Detection of a submerged object insonified by surface noise in an ocean waveguide

Nicholas C. Makris
Naval Research Laboratory, Washington, DC 20375

Frank Ingenito
SACLANT Undersea Research Centre, La Spezia, Italy

William A. Kuperman
Scripps Institution of Oceanography, La Jolla, California 92093

(Received 24 December 1993; accepted for publication 23 May 1994)

A theory is developed and applied to determine whether an object submerged in an ocean waveguide and insonified only by surface-generated noise can be detected with conventional sensing arrays. An expression for the total noise-field covariance of a stratified waveguide with a submerged object present is derived using full-field wave theory. This is evaluated by numerical wave-number integration for a spherical object in a shallow water waveguide. The Cramer–Rao lower bound on detection error is computed for several realistic shallow water scenarios at both low and high frequency. The results indicate that cross-range localization is possible when the array aperture is sufficient to resolve the object scale. This conclusion is supported by beamforming simulations. Range localization is possible at greater distances. However, this requires high correlation between direct and scattered noise fields at the sensor, which is difficult to replicate via matched field processing. In addition, wave theory indicates that high resolution imaging of reflected ambient noise is generally most effective within the deep shadow range of the object. Beyond the deep shadow range, diffractive interference from the total forward field may overwhelm reflections, depending upon the incident noise directional spectrum and measurement range. Overall, present analysis indicates that the proposed detection scheme presses the limits of current technology.

PACS numbers: 43.30.Nb, 43.30.Wi, 43.30.Ft

INTRODUCTION

We investigate the possibility of detecting a submerged object insonified only by surface noise in an ocean waveguide at ranges which may be much greater than an object dimension. We do so by means of stochastic noise modeling, wave and scattering theory, as well as detection techniques which are widely used in the underwater acoustics community. Our motivation in this effort is twofold. First, we are interested in alternative methods for passive detection of underwater objects. Second, we are interested in the ability of submerged vehicles and marine mammals to perceive their environment. For example, can dolphins acoustically image prey without relying upon their ability to actively insonify a target?

Our problem is expected to have extremely low signal-to-noise ratio (SNR) beyond the immediate vicinity of the object. This is because the noise field incident on an object is of the same order as the direct noise field measured at any observation point. However, the scattered noise field is reduced by spreading, scattering and absorption. If the coherence scale of the noise at the sensor has been augmented by the object's presence, localization by coherent processing may be possible. In order to separate scattered from direct noise, which is assumed to be azimuthally homogeneous, the coherence scale may have to extend over an aperture sufficient to resolve the object. Detection is then highly dependent upon the SNR, array gain and sidelobe level of the sensing device. Since these have no simple geometric relationship to object dimension, range and array aperture in a waveguide, the best way to judge the practicality of the concept is via modeling and simulation.

To our knowledge, the first documented discussion of using naturally occurring ambient noise in the ocean as an analogy to "daylight" appears in a 1985 article.[1] Here, and in a follow-up paper,[2] the possibility of detecting submarines solely by their noise absorbing and scattering properties is investigated by preliminary approximations. More recent experimental,[3] and theoretical,[4] results indicate the possibility of detecting a submerged object using high frequency ambient noise. Extremely short range detections, within 10 m of a 3-m object, were made in the high frequency range of 5 to 45 kHz near a beach with a large pier. The experiment used a parabolic reflector directed at a rectangular object. Directional variations were not reported, but only the difference in ambient noise level for differing orientations of the object, reflector and beach. In the present paper, we find support for these high frequency experimental results and explore the possibility of detection at much longer ranges and lower frequencies with full-field modeling in a realistic shallow water environment.

Our theoretical formulation is exact for arbitrary range and frequency given the exact scattering function for the specific object and environment. In order to make the problem more tractable for practical considerations we have adopted a single simplifying approximation. We use the free-space

Redistribution subject to ASA license or copyright; see http://acousticalsociety.org/content/terms. Download to IP: 18.38.0.166 On: Mon, 12 Jan 2015 18:30:17

scattering function of the object.[5] This ignores contributions from multiple scattering and is valid for objects not too close to surface and bottom boundaries. This approximation does not significantly affect the accuracy nor limit the range or frequency domain of interest for most ocean acoustic applications.

We adopt a fully stochastic approach in our theoretical formulation, following the noise modelling of Ref. 6. This avoids biases and inaccuracies associated with the alternative approach of using statistical realizations to represent the noise sources. The stochastic approach is also convenient since the spatial covariance of the total noise field on the sensing array is the quantity directly required for detection. Specifically, an object is placed in the correlated noise field of a three-dimensional ocean waveguide.[7] The noise field is generated by a continuous sheet of stochastic sources below the free surface which extend uniformly in range and azimuth from the object. The azimuthal directionality of the noise field is therefore homogeneous. (Preliminary results indicate that azimuthally inhomogeneous noise, in the presence of a coastline with surf, for example, may be far more advantageous to detection.[8] However, we reserve more thorough analysis of this for a future article.)

We accommodate sources near the object in Sec. I by modifying a previously developed theory for scattering from an object in a stratified waveguide.[5] The former theory is in terms of normal modes and is therefore more appropriate for large range separations between noise source and scatterer. While contributions from nearby surface sources can be incorporated by artificially extending the basement layer to approximate continuum modes, we model them precisely with an alternative approach. We develop a spectral representation for the scattered field using the methodology of Ref. 5. In Sec. II, we then integrate the scattered and direct field contributions from the ensemble of stochastic surface sources. This leads to an expression for the spatial covariance of the total noise field in terms of multidimensional wave number integrals for an arbitrary object. These integrals are decomposed into the sum of the scattered, direct and respective cross covariance contributions to the total noise field. In Sec. III, we introduce the free-space scattering function of a spherical object. Spherical symmetry enables us to reduce these covariance terms to the sum and product of separate one-dimensional wave number integrals. These expressions are then evaluated by numerical integration for some illustrative examples using a typical shallow water waveguide. The spatial characteristics and coherence structure of the noise is then investigated.

In Sec. IV, we simulate detection for various ranges and frequencies using conventional arrays and signal processing techniques. Limitations on detection and imaging imposed by diffraction are discussed here and in Appendix C. We then compute the theoretical lower bound on object localization error for the given arrays using the Cramer–Rao approach. This gives the upper bound on performance and provides a synoptic guide to some situations in which detection by scattered surface noise is possible.

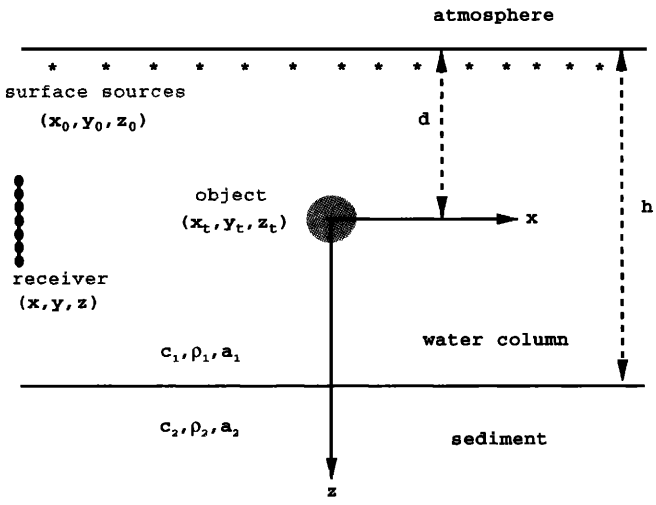

FIG. 1. The geometry and coordinates of a submerged object in a Pekeris waveguide with surface generated noise. All coordinate systems have origin at the object center with positive z pointing downward. The waveguide depth is h, the depth of the object center is d. The sound speed, density and attenuation of the water column and sediment are c_1, ρ_1, a_1 and c_2, ρ_2, a_2, respectively.

I. FULL-FIELD SCATTERING FROM AN OBJECT IN A WAVEGUIDE

In our generalized stochastic formulation, we model sources of surface noise as extending continuously in range and azimuth from a submerged object in an ocean environment. However, the expressions for the field scattered from an object in a waveguide of Ref. 5 are most appropriate for large source ranges since they are in terms of normal modes. To remedy this, we derive similar expressions in this section which are valid for arbitrary source range by reformulating the scattered field in terms of wave-number integrals.

We use the following notation: (x_0,y_0,z_0) are the source coordinates; (x_t,y_t,z_t) are coordinates on the surface of the object; and (x,y,z) are the field coordinates. The origin for all of these coordinate systems is at the center of the object with positive z pointing downward. Cylindrical (ρ,θ,z) and spherical (r,θ,ϕ) coordinates are defined as follows

$$x_0 = r_0 \sin\theta_0 \cos\phi_0, \quad x_t = r_t \sin\theta_t \cos\phi_t,$$

$$x = r \sin\theta \cos\phi,$$

$$y_0 = r_0 \sin\theta_0 \sin\phi_0, \quad y_t = r_t \sin\theta_t \sin\phi_t,$$

$$y = r \sin\theta \sin\phi,$$

$$z_0 = r_0 \cos\theta_0, \quad z_t = r_t \cos\theta_t, \quad z = r \cos\theta,$$

$$\rho_0^2 = x_0^2 + y_0^2, \quad \rho_t^2 = x_t^2 + y_t^2, \quad \rho^2 = x^2 + y^2.$$

The geometry of an object submerged in a waveguide with surface generated noise is shown in Fig. 1. For consistency with the simulations to follow, the specified geometry is that of a shallow water Pekeris waveguide, although the form of the solution is later generalized to include water column stratification. The geometry of respective spatial and wave-number coordinate systems is shown in Fig. 2.

We express the total field $\Phi(\mathbf{r})$ as the sum of the incident field $\Phi_i(\mathbf{r})$ and the scattered field $\Phi_S(\mathbf{r})$,

Redistribution subject to ASA license or copyright; see http://acousticalsociety.org/content/terms. Download to IP: 18.38.0.166 On: Mon, 12 Jan 2015 18:30:17

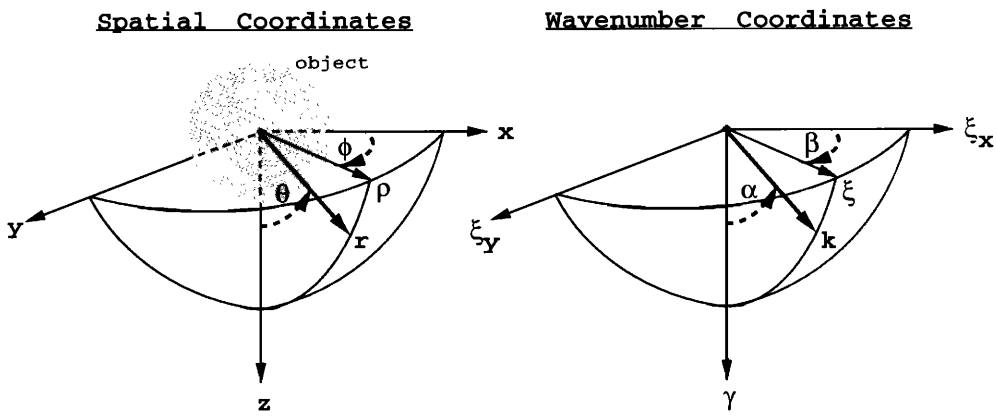

FIG. 2. The geometry of spatial and wave-number coordinates. All coordinate systems have origin at the object center.

$$\Phi(\mathbf{r})=\Phi_i(\mathbf{r})+\Phi_S(\mathbf{r}), \tag{1}$$

and begin with Eq. (37) of Ref. 5 for the scattered field from a rigid surface with unspecified shape

$$\Phi_s(\mathbf{r})=-\int\int_A[\Phi_i(\mathbf{r}_t)+\Phi_s(\mathbf{r}_t)]\frac{\partial}{\partial \mathbf{n}_t}G(\mathbf{r}|\mathbf{r}_t)d\mathbf{A}_t, \tag{2}$$

where $G(\mathbf{r}|\mathbf{r}_t)$ is the waveguide Green's function, $\Phi_i(\mathbf{r}_t)$ is the field incident on the object, and $\Phi_S(\mathbf{r}_t)$ is the scattered field on the object.

We then decompose the incident field into plane waves,

$$\Phi_i(\mathbf{r}_t)=\frac{1}{2\pi}\int d^2\boldsymbol{\xi}_i\, g(\xi_i;z_t,z_0)e^{-i\boldsymbol{\xi}_i\cdot(\boldsymbol{\rho}_t-\boldsymbol{\rho}_0)}, \tag{3}$$

where $g(\xi_i;z,z_0)$ satisfies

$$\frac{dg}{dz^2}+[k(z)^2-\xi_i^2]g=-\frac{1}{2\pi}\delta(z-z_0), \tag{4}$$

and

$$\gamma_i=\sqrt{[k^2(z)-\xi_i^2]}, \quad \text{for } k^2(z)\geqslant\xi_i^2,$$
$$=i\sqrt{[\xi_i^2-k^2(z)]}, \quad \text{for } k^2(z)<\xi_i^2, \tag{5}$$

is the vertical wave-number magnitude in the water column, and $k(z)=\omega/c_1+ia_1$, where ω is the angular frequency, c_1 and a_1 are the sound speed and attenuation of the water column. After boundary conditions appropriate to the waveguide are satisfied (see Fig. 1) the following wave-number-depth Green's function solution results for $h-d\geqslant z_t\geqslant z_0$

$$g(\xi_i;z_t,z_0)=A(z_0)e^{i\gamma_i z_t}+B(z_0)e^{-i\gamma_i z_t}, \tag{6}$$

where

$$A(z_0)=\frac{1}{4\pi i\gamma_i}\left(\frac{e^{i\gamma_i(z_0+2d)}-e^{-i\gamma_i z_0}}{1-R_{si}R_{bi}e^{2i\gamma_i h}}\right) \tag{7a}$$

and

$$B(z_0)=\frac{-R_{si}R_{bi}e^{2i\gamma_i h}}{4\pi i\gamma_i}\left(\frac{e^{i\gamma_i z_0}-e^{-i\gamma_i(z_0+2d)}}{1-R_{si}R_{bi}e^{2i\gamma_i h}}\right). \tag{7b}$$

Both factors are in terms of the surface and bottom reflection coefficients R_{si} and R_{bi} for the incident field where

$$R_{si}=-1, \tag{8a}$$

$$R_{bi}=\frac{\rho_2\gamma_i/(\rho_1\vartheta_i)-1}{\rho_2\gamma_i/(\rho_1\vartheta_i)+1}. \tag{8b}$$

The vertical wave-number magnitude in the sediment is

$$\vartheta_i=\sqrt{[k^2(z)-\xi_i^2]}, \quad \text{for } k^2(z)\geqslant\xi_i^2,$$
$$=i\sqrt{[\xi_i^2-k^2(z)]}, \quad \text{for } k^2(z)<\xi_i^2, \tag{9}$$

where $k(z)=\omega/c_2+ia_2$, and c_2 and a_2 are the sound speed and attenuation of the sediment. Substituting Eq. (6) back into Eq. (3) we have the field incident on the object in terms of up and down going plane waves

$$\Phi_i(\mathbf{r}_t)=\frac{1}{2\pi}\int d^2\boldsymbol{\xi}_i[A(z_0)e^{i(-\boldsymbol{\xi}_i\cdot\boldsymbol{\rho}_t+\gamma_i z_t)}$$
$$+B(z_0)e^{i(-\boldsymbol{\xi}_i\cdot\boldsymbol{\rho}_t-\gamma_i z_t)}]e^{i\boldsymbol{\xi}_i\cdot\boldsymbol{\rho}_0}. \tag{10}$$

Similarly, we decompose the waveguide Green's function into plane waves

$$G(\mathbf{r}|\mathbf{r}_t)=\frac{1}{2\pi}\int d^2\boldsymbol{\xi}\, g(\xi;z,z_t)e^{i\boldsymbol{\xi}\cdot(\boldsymbol{\rho}-\boldsymbol{\rho}_t)}, \tag{11}$$

where

$$g(\xi;z_t,z)=C(z)e^{i\gamma z_t}+D(z)e^{-i\gamma z_t}, \quad \text{for } h-d\geqslant z\geqslant z_t,$$
$$=A(z)e^{i\gamma z_t}+B(z)e^{-i\gamma z_t}, \quad \text{for } z_t>z\geqslant -d, \tag{12}$$

and

$$C(z)=\frac{1}{4\pi i\gamma}\left(\frac{e^{i\gamma(z+2d)}-R_sR_be^{2i\gamma h}e^{-i\gamma z}}{1-R_sR_be^{2i\gamma h}}\right), \tag{13a}$$

$$D(z)=-\frac{1}{4\pi i\gamma}\left(\frac{e^{i\gamma z}-R_sR_be^{2i\gamma h}e^{-i\gamma(z+2d)}}{1-R_sR_be^{2i\gamma h}}\right). \tag{13b}$$

The incident field subscripts are no longer appropriate and have been dropped.

Now both the incident field on the object $\Phi_i(\mathbf{r}_t)$ and the waveguide Green's function $\mathbf{G}(\mathbf{r}|\mathbf{r}_t)$ are expressed in terms of up and down going plane waves. Substituting these back into Eq. (2) we have

Redistribution subject to ASA license or copyright; see http://acousticalsociety.org/content/terms. Download to IP: 18.38.0.166 On: Mon, 12 Jan 2015 18:30:17

$$\Phi_s(\mathbf{r}) = -\int\int_A \left(\frac{1}{2\pi} \int d^2\xi_i \, e^{i\xi_i\cdot\rho_0} [A(z_0) e^{i(-\xi_i\cdot\rho_t + \gamma_i z_t)} + B(z_0) e^{i(-\xi_i\cdot\rho_t - \gamma_i z_t)}] + \Phi_s(\mathbf{r}_t) \right) \times \frac{\partial}{\partial \mathbf{n}_t} \left(\frac{1}{2\pi} \int d^2\xi \, e^{i\xi\cdot\rho} [C(z) e^{i(-\xi\cdot\rho_t + \gamma z_t)} + D(z) e^{i(-\xi\cdot\rho_t - \gamma z_t)}] \right) d\mathbf{A}_t . \tag{14}$$

To incorporate a plane-wave scattering function, we express the wave-number components in terms of their associated propagation angles, which may be complex. Once again, the origin of these coordinate systems is at the center of the object. A geometrical interpretation of the following expressions has been provided in Fig. 2,

$$\begin{aligned} \xi_{ix} &= k \sin\alpha_i \cos\beta_i, \quad \xi_x = k \sin\alpha \cos\beta, \\ \xi_{iy} &= k \sin\alpha_i \sin\beta_i, \quad \xi_y = k \sin\alpha \sin\beta, \\ \gamma_i &= k \cos\alpha_i, \quad \gamma = k \cos\alpha, \\ \xi_i^2 &= \xi_{ix}^2 + \xi_{iy}^2, \quad \xi^2 = \xi_x^2 + \xi_y^2. \end{aligned} \tag{15}$$

For example, $\boldsymbol{\xi}\cdot\boldsymbol{\rho} + \gamma z = kr\,\eta(\alpha,\beta;\theta,\phi)$, where

$$\eta(\alpha,\beta;\theta,\phi) = \cos\alpha\cos\theta + \sin\alpha\sin\theta\cos(\beta-\phi), \tag{16}$$

is the cosine of the angle between the propagation direction (α,β) and field coordinate direction (θ,ϕ). Substituting these into Eq. (14) we have

$$\Phi_s(\mathbf{r}) = -\int\int_A \left(\frac{1}{2\pi} \int d^2\xi_i \, e^{i\xi_i\cdot\rho_0} [A(z_0) e^{-ikr_t\eta(\pi-\alpha_i,\beta_i;\theta_t,\phi_t)} + B(z_0) e^{-ikr_t\eta(\alpha_i,\beta_i;\theta_t,\phi_t)}] + \Phi_s(\mathbf{r}_t) \right) \times \frac{\partial}{\partial \mathbf{n}_t} \left(\frac{1}{2\pi} \int d^2\xi \, e^{i\xi\cdot\rho} [C(z) e^{-ikr_t\eta(\pi-\alpha,\beta;\theta_t,\phi_t)} + D(z) e^{-ikr_t\eta(\alpha,\beta;\theta_t,\phi_t)}] \right) dA_t , \tag{17}$$

for $h-d \geq z \geq z_t$. We can then express the scattered field in the waveguide in terms of a plane-wave scattering function $\mathsf{S}(\theta,\phi;\theta_i,\phi_i)$ for the object

$$\Phi_s(\mathbf{r}) = \frac{1}{\pi k} \int\int d^2\xi \, d^2\xi_i \, e^{i[\xi_i\cdot\rho_0 + \xi\cdot\rho]} F(z,z_0;\xi,\xi_i), \tag{18}$$

where

$$\begin{aligned} F(z,z_0;\xi,\xi_i) = \{ & A(z_0)C(z)\mathsf{S}(\pi-\alpha,\beta;\pi-\alpha_i,\beta_i) \\ & + A(z_0)D(z)\mathsf{S}(\alpha,\beta;\pi-\alpha_i,\beta_i) \\ & + B(z_0)C(z)\mathsf{S}(\pi-\alpha,\beta;\alpha_i,\beta_i) \\ & + B(z_0)D(z)\mathsf{S}(\alpha,\beta;\alpha_i,\beta_i)\}, \end{aligned} \tag{19}$$

for $h-d \geq z \geq z_t$. For $z_t > z \geq -d$, substitute $A(z)$ for $C(z)$ and $B(z)$ for $D(z)$ in Eq. (19) above.

The above expression is the exact solution for the scattered field if $\mathsf{S}(\theta,\phi;\theta_i,\phi_i)$ is the scattering function for the specific object with mixed boundary conditions in the specific waveguide. The expression is generalized to a stratified water column by reformulating the local planewave amplitudes A,B,C,D to include the appropriate object depth dependence. However, the approximation that the index of refraction is constant over the object must be valid.

It is difficult to obtain an exact expression for $\mathsf{S}(\theta,\phi;\theta_i,\phi_i)$. Therefore, we approximate $\mathsf{S}(\theta,\phi;\theta_i,\phi_i)$ by the free-space plane-wave scattering function[9] $S(\theta,\phi;\theta_i,\phi_i)$ which is most easily interpreted in the far field where

$$\Phi_s(\mathbf{r}) \approx \left(\frac{e^{ikr}}{kr} \right) S(\theta,\phi;\theta_i,\phi_i) \tag{20}$$

is the scattered field at (θ,ϕ) for an incident plane wave propagating in the direction (θ_i,ϕ_i). By introducing the free-space scattering function, we use the same reasoning as in Sec. III of Ref. 5. The scattered field on the surface of the object is approximated by the scattered field on the surface of the object in free space. This is valid so long as multiple reflections between object and waveguide boundaries are not important, i.e. if the object is not too close to boundaries. If we substitute $S(\theta,\phi;\theta_i,\phi_i)$ for $\mathsf{S}(\theta,\phi;\theta_i,\phi_i)$ in Eq. (19), then the resulting expression is exact, neglecting multiple scattering.

II. SURFACE NOISE FIELD COVARIANCE FOR A STRATIFIED OCEAN WAVEGUIDE WITH A SUBMERGED OBJECT

The spatial covariance of the surface-generated noise field is derived in this section for a stratified ocean waveguide with a submerged object present. This is done by combining the wave theory of the previous section with a stochastic model for the surface sound sources. We use the approach of Ref. 6, and represent surface noise sources by a continuous sheet of random monopoles at z_0 below the pressure-release surface. To simplify our derivation, we express the total noise field as a sum of two parts. The first part $\Psi_N(\mathbf{r})$ is the noise field measured in the absence of the object, which we refer to as the direct noise field. The second part $\Psi_S(\mathbf{r})$ is the surface noise scattered from the object in the waveguide, which we refer to as the scattered noise field. The spatial covariance of the total noise field in the presence of the object is then

$$C(\mathbf{r},\mathbf{r}') = \langle [\Psi_N(\mathbf{r}) + \Psi_S(\mathbf{r})][\Psi_N(\mathbf{r}') + \Psi_S(\mathbf{r}')]^* \rangle . \tag{21}$$

Redistribution subject to ASA license or copyright; see http://acousticalsociety.org/content/terms. Download to IP: 18.38.0.166 On: Mon, 12 Jan 2015 18:30:17

This can be decomposed into the following terms:

$$C(\mathbf{r},\mathbf{r}')=C_{NN}(\mathbf{r},\mathbf{r}')+C_{NS}(\mathbf{r},\mathbf{r}')+C_{SN}(\mathbf{r},\mathbf{r}') + C_{SS}(\mathbf{r},\mathbf{r}'), \tag{22}$$

where $C_{NN}(\mathbf{r},\mathbf{r}') = \langle \Psi_N(\mathbf{r})\Psi_N^*(\mathbf{r}')\rangle$ is the covariance of the direct noise field; $C_{SS}(\mathbf{r},\mathbf{r}') = \langle \Psi_S(\mathbf{r})\Psi_S^*(\mathbf{r}')\rangle$ is the covariance of the scattered noise field; and $C_{NS}(\mathbf{r},\mathbf{r}') = \langle \Psi_N(\mathbf{r})\Psi_S^*(\mathbf{r}')\rangle$ is the covariance between the direct and scattered noise field. Since the total noise field covariance must be Hermitian, it follows that

$$C_{NS}(\mathbf{r},\mathbf{r}')=C_{SN}^*(\mathbf{r}',\mathbf{r}). \tag{23}$$

We first derive the covariance of the scattered noise field by integrating contributions from the infinite sheet of surface sources,

$$C_{SS}(\mathbf{r},\mathbf{r}')=\int\int d^2\mathbf{r}_0\, d^2\mathbf{r}_0'\langle S_\omega(\mathbf{r}_0)S_\omega^*(\mathbf{r}_0')\rangle \times \phi_s(\mathbf{r},\mathbf{r}_0)\phi_s^*(\mathbf{r}',\mathbf{r}_0'), \tag{24}$$

where $S_\omega(\mathbf{r}_0)$ is the Fourier transform of the noise source time dependence at angular frequency ω over the time interval T. Following Ref. 6, we assume that the spatial coherence of the noise sources depends only upon their separation and that they are uncorrelated

$$\langle S_\omega(\mathbf{r}_0)S_\omega^*(\mathbf{r}_0')\rangle=\frac{2q^2}{k^2}\,\frac{\delta(|\mathbf{r}_0'-\mathbf{r}_0|)}{|\mathbf{r}_0'-\mathbf{r}_0|}, \tag{25}$$

where q^2/T is the source-strength spectral density of the monopole sheet. Substituting Eq. (25) and Eq. (18) into Eq. (24), and changing variables so that $\boldsymbol{\rho}_0' = \mathbf{R} + \boldsymbol{\rho}_0$, we can eliminate the surface integral in $\mathbf{R}$ to obtain

$$C_{SS}(\mathbf{r},\mathbf{r}')=2\pi\left(\frac{2q^2}{k^2}\right)\times\left(\frac{1}{\pi k}\right)^2\int\int\int\int d^2\boldsymbol{\xi}_i\, d^2\boldsymbol{\xi}_i'\, d^2\boldsymbol{\xi}\, d^2\boldsymbol{\xi}', F(z,z_0;\boldsymbol{\xi},\boldsymbol{\xi}_i)F^*(z',z_0;\boldsymbol{\xi}',\boldsymbol{\xi}_i')e^{i[\boldsymbol{\xi}\cdot\mathbf{r}-\boldsymbol{\xi}'\cdot\mathbf{r}']} \times\int d^2\boldsymbol{\rho}_0\, e^{i[\boldsymbol{\xi}_i-\boldsymbol{\xi}_i']\cdot\boldsymbol{\rho}_0}. \tag{26}$$

Recognizing that

$$\int d^2\boldsymbol{\rho}_0\, e^{i[\boldsymbol{\xi}_i-\boldsymbol{\xi}_i']\cdot\boldsymbol{\rho}_0}=(2\pi)^2\delta(\xi_{ix}-\xi_{ix}')\delta(\xi_{iy}-\xi_{iy}'), \tag{27}$$

we arrive at a six-dimensional wave-number integral

$$C_{SS}(\mathbf{r},\mathbf{r}')=(2\pi)^3\left(\frac{2q^2}{k^2}\right)\left(\frac{1}{\pi k}\right)^2\int\int\int d^2\boldsymbol{\xi}_i \times d^2\boldsymbol{\xi}\, d^2\boldsymbol{\xi}'\, F(z,z_0;\boldsymbol{\xi},\boldsymbol{\xi}_i) \times F^*(z',z_0;\boldsymbol{\xi}',\boldsymbol{\xi}_i)e^{i[\boldsymbol{\xi}\cdot\boldsymbol{\rho}-\boldsymbol{\xi}'\cdot\boldsymbol{\rho}']}, \tag{28}$$

which cannot be simplified further without knowledge of the scattering function of the object and the acoustic properties of the waveguide.

Similarly we obtain the following expression for the covariance between the scattered and direct noise fields:

$$C_{SN}(\mathbf{r},\mathbf{r}')=(2\pi)^2\left(\frac{2q^2}{k^2}\right)\times\left(\frac{1}{\pi k}\right)\int\int d^2\boldsymbol{\xi}\, d^2\boldsymbol{\xi}'\, F(z,z_0;\boldsymbol{\xi},\boldsymbol{\xi}') \times g^*(z',z_0;\boldsymbol{\xi}')e^{i[\boldsymbol{\xi}\cdot\boldsymbol{\rho}+\boldsymbol{\xi}'\cdot\boldsymbol{\rho}']}, \tag{29}$$

where $C_{NS}(\mathbf{r},\mathbf{r}')$ is available via Eq. (23).

Finally, the direct noise field covariance is available from Ref. 6,

$$C_{NN}(\mathbf{r},\mathbf{r}')=(2\pi)^2\left(\frac{2q^2}{k^2}\right)\times\int_0^\infty \xi\, d\xi\, g(\xi;z,z_0)g^*(\xi;z',z_0)J_0(\xi|\boldsymbol{\rho}'-\boldsymbol{\rho}|). \tag{30}$$

We note that for receivers at the same depth, the direct noise field covariance is real, and is only a function of horizontal separation.

III. SURFACE NOISE FIELD COVARIANCE FOR A STRATIFIED OCEAN WAVEGUIDE WITH A SUBMERGED SPHERICAL OBJECT

Using the expressions developed in the previous section, and the relevant free-space scattering function, we derive the total noise field covariance for a stratified ocean waveguide with a submerged spherical object. We choose a sphere principally because spherical symmetry enables the multidimensional integrals for the scattered noise field to be reduced to a combination of one-dimensional wave-number integrals which are easily evaluated numerically. In this section we present the general solution and some illustrative examples. The derivation is outlined in Appendix A.

A. General solution

We introduce the following notation, which employs standard symbols for Bessel and Legendre functions. One dimensional wave-number integrals with subscripts A or B are of the form

$$I_{BA}(n,l)=\int_0^\infty \xi_i\, d\xi_i B(z_0)A^*(z_0)P_n\left(\frac{\gamma_i}{k}\right)P_l^*\left(\frac{\gamma_i}{k}\right), \tag{31a}$$

$$\mathfrak{I}_{BA}(n,l,m)=\int_0^\infty \xi_i\, d\xi_i B(z_0)A^*(z_0)P_n^m\left(\frac{\gamma_i}{k}\right)P_l^{m*}\left(\frac{\gamma_i}{k}\right). \tag{31b}$$

Integrals with subscripts C or D are of the form

Redistribution subject to ASA license or copyright; see http://acousticalsociety.org/content/terms. Download to IP: 18.38.0.166 On: Mon, 12 Jan 2015 18:30:17

$$I_{CD}(\rho,z;n)=\int_0^\infty \xi\, d\xi\, C(z)P_n\left(\frac{\gamma}{k}\right)J_0(\rho\xi) + \int_0^\infty \xi\, d\xi\, D(z)P_n\left(-\frac{\gamma}{k}\right)J_0(\rho\xi), \quad (32a)$$

$$\mathfrak{I}_{CD}(\rho,z;n,m)=\int_0^\infty \xi\, d\xi\, C(z)P_n^m\left(\frac{\gamma}{k}\right)J_m(\rho\xi) + \int_0^\infty \xi\, d\xi\, D(z)P_n^m\left(-\frac{\gamma}{k}\right)J_m(\rho\xi). \quad (32b)$$

And integrals with subscripts A or B and g are of the form

$$I_{Ag}(\rho',z';n)=\int_0^\infty \xi'\, d\xi'\, J_0(\xi'\rho') \times P_n\left(\frac{\gamma'}{k}\right)A(z_0)g^*(z',z_0;\xi'), \quad (33a)$$

$$\mathfrak{I}_{Ag}(\rho',z';n,m)=\int_0^\infty \xi'\, d\xi'\, J_m(\xi'\rho') \times P_n^m\left(\frac{\gamma'}{k}\right)A(z_0)g^*(z',z_0;\xi'). \quad (33b)$$

The covariance of the scattered noise field is then

$$C_{SS}(\mathbf{r},\mathbf{r}')=(2\pi)^6\left(\frac{2q^2}{k^2}\right)\left(\frac{1}{\pi k}\right)^2\sum_{n=0}^\infty\sum_{l=0}^\infty f(n)f^*(l)\Big([I_{AA}(n,l)I_{CD}(\rho,z;n)I_{CD}^*(\rho',z';l) + I_{BA}(n,l)I_{DC}(\rho,z;n)I_{CD}^*(\rho',z';l)+I_{AB}(n,l)I_{CD}(\rho,z;n)I_{DC}^*(\rho',z';l)+I_{BB}(n,l)I_{DC}(\rho,z;n)I_{DC}^*(\rho',z';l)] + 2\sum_{m=1}^{\min(l,n)}\frac{(n-m)!}{(n+m)!}\frac{(l-m)!}{(l+m)!}\cos m(\phi-\phi')[\mathfrak{I}_{AA}(n,l,m)\mathfrak{I}_{CD}(\rho,z;n,m)\mathfrak{I}_{CD}^*(\rho',z';l,m) + \mathfrak{I}_{BA}(n,l,m)\mathfrak{I}_{DC}(\rho,z;n,m)\mathfrak{I}_{CD}^*(\rho',z';l,m)+\mathfrak{I}_{AB}(n,l,m)\mathfrak{I}_{CD}(\rho,z;n,m)\mathfrak{I}_{DC}^*(\rho',z';l,m) + \mathfrak{I}_{BB}(n,l,m)\mathfrak{I}_{DC}(\rho,z;n,m)\mathfrak{I}_{DC}^*(\rho',z';l,m)]\Big), \quad (34)$$

and the covariance between the scattered and direct noise field is

$$C_{SN}(\mathbf{r},\mathbf{r}')=(2\pi)^4\left(\frac{2q^2}{k^2}\right)\left(\frac{1}{\pi k}\right)\sum_{n=0}^\infty f(n)\Big([I_{Ag}(\rho',z';n)I_{CD}(\rho,z;n)+I_{Bg}(\rho',z';n)I_{DC}(\rho,z;n)] + 2\sum_{m=1}^{n}\frac{(n-m)!}{(n+m)!}\cos m(\phi-\phi')[\mathfrak{I}_{Ag}(\rho',z';n)\mathfrak{I}_{CD}(\rho,z;n,m)+\mathfrak{I}_{Bg}(\rho',z';n)\mathfrak{I}_{DC}(\rho,z;n,m)]\Big), \quad (35)$$

where $C_{NS}(\mathbf{r},\mathbf{r}')$ can be obtained by Eq. (23).

For a rigid sphere we have

$$f(n)=i(-1)^n(2n+1)\frac{j_n'(ka)}{h_n^{(1)'}(ka)}, \quad (36)$$

and for a pressure-release or soft sphere

$$f(n)=i(-1)^n(2n+1)\frac{j_n(ka)}{h_n^{(1)}(ka)}. \quad (37)$$

Equations (31)–(35) are for $h-d\geq z\geq z_t$. For $z_t>z\geq -d$, substitute $A(z)$ for $C(z)$ and $B(z)$ for $D(z)$ in Eqs. (32a)–(32b).

In Equations (34) and (35), the solutions are expressed as a sum of two sets of terms as a result of the addition theorem for spherical harmonics. The first set gives the azimuthally omnidirectional component and is comprised of sums over zero-order Bessel functions J_0 and Legendre polynomials P_n of degree n. The second set of terms gives the azimuthally directional component and is comprised of summations of higher order Bessel functions J_m and the associated higher-order Legendre polynomials P_n^m. The A, B, C and D factors scale local plane-wave components of the wave number-depth Green's function and include information about waveguide stratification. [The solution to the Pekeris problem is obtained by substituting the respective expressions for these given in Eqs. (7) and (13).] These factors are weighted by the proper Legendre polynomial, to give the directional characteristics of the scatterer, and are converted to field coordinates by a standard Bessel transform of the above integrals. The asymptotic form of the spherical Bessel and Hankel functions, and their derivatives, may be used in Eqs. (36) and (37) for the large and small ka cases respectively when the order of the function allows this. Assymp-

Redistribution subject to ASA license or copyright; see http://acousticalsociety.org/content/terms. Download to IP: 18.38.0.166 On: Mon, 12 Jan 2015 18:30:17

totically large ka can lead to smoother peaks in the wave-number spectrum and a more stable numerical integration than for a point source at the same frequency.

The intensities of the scattered noise field, direct noise field and total noise field are denoted by $I_s(\mathbf{r})$, $I_N(\mathbf{r})$, and $I(\mathbf{r})$, respectively. These are obtained by frequency integration of the respective covariances $C_{SS}(\mathbf{r},\mathbf{r})$, $C_{NN}(\mathbf{r},\mathbf{r})$, and $C(\mathbf{r},\mathbf{r})$. For example, the bandlimited scattered noise intensity about center frequency f_0 is

$$I_S(\mathbf{r})=\left(\frac{1}{\rho c}\right)\left(\frac{1}{T}\right)\int_{f_0-\Delta f/2}^{f_0+\Delta f/2} C_{SS}(\mathbf{r},\mathbf{r})df.$$

We adopt the convention that the source-strength spectral density is normalized to unity such that $10\log(q^2/T)=0$ dB *re*:1 μPa^2/(Hz m^2). (Notice that μPa m units are consistent with a standard monopole source strength, but in our case are also divided by areal units for the continuous sheet.) When the covariances are integrated as above over a uniform Δf =1-Hz band, $10\log[\rho c I_S(\mathbf{r})]$ has sound pressure level (SPL) units in dB *re*:1 μPa.

B. Illustrative examples

We present numerical simulations illustrating the intensity of the scattered, direct, and total noise field as well as the azimuthal coherence $R_{SS}(\rho,\Delta\phi)$ which is defined in Appendix B. These examples give a quantitative description of the spatial characteristics of the SNR as a function of range and depth from the object and the azimuthal coherence scale of the scattered noise field. This information is important in designing the sensor aperture and determining the array gain necessary for detection.

All simulations are derived by numerical wave-number integration of Eqs. (30), (34), and (35), for the shallow-water waveguide shown in Fig. 1. The surface noise sources are submerged within a quarter wavelength of the free surface. Each source produces the dipole radiation pattern consistent with low to mid-frequency field observations.[10] (High-frequency field observations are too sparse to be included.) For example, at low frequency, the radiation pattern produced by this source placement can replicate that of a bubble concentration near the free surface which rapidly decays with depth.[11] This is also the case at higher frequencies for shallow grazing-angle propagation, typical in a shallow waveguide, so long as the bubbles remain acoustically compact. In either case, only the absolute level needs to be scaled.[12] However, the absolute scale is unimportant for our detection problem because the scattered noise intensity is proportional to the direct noise intensity.

The noise sources insonify a sphere which is always in the center of the waveguide at $z=0$. The water column and sediment parameters are fixed at $c_1=1500$ m/s, $\rho_1=1000$ kg/m^3, $c_2=1700$ m/s, $\rho_2=1900$ kg/m^3, $a_2=(0.1/\lambda)$ m^{-1}. Low and high-frequency examples are presented for soft and rigid boundary conditions on the sphere. For the low-frequency cases the sources are at $z_0=0.5-d$ meters, where $h=100$ m and $d=50$ m. The sphere's radius is $a=10$ m. A water column attenuation of $a_1=7.0\times10^{-8}$ m^{-1} is used for the $f=50$ Hz case where $ka\approx2$; and a water column attenuation of $a_1=1.4\times10^{-5}$ m^{-1} is used for $f=300$ Hz where $ka\approx12.6$. For the high-frequency $f=10$ kHz case, the sources are at $z_0=0.01875-d$ meters; the sphere's radius is reduced to $a=0.25$ m, $ka\approx10.5$; and the water column attenuation is increased to $a_1=0.0003$ m^{-1}.

We first consider the scattered noise intensities shown in Fig. 3 for pressure release boundary conditions on the spheres. (The corresponding scattered intensities from rigid spheres are not significantly different except for the 50-Hz case where the overall levels are slightly lower.) For the 50-Hz example, modal structure in the waveguide is evident. At 300 Hz, waveguide interference is less evident. For the 10-kHz case, a diffuse beampattern emerges from the object with asymmetric directional variations about the horizontal related to those of the incident noise field. Here, the rapid falloff in intensity with increasing range from the object is due to the dramatic decrease in a/h and λ/h. As a result, waveguide interference is not evident over the short range shown. At higher frequency, the combination of higher volumetric absorption in the water column and sediment, as well as increased bottom interaction, will significantly reduce the scattered intensity at increasing range. This is evident when the transmission loss at 1-km range is compared for the 50- and 300-Hz cases, where the sphere size remains constant. For comparison, we also present the SPL due to monopole point sources placed at the center of the waveguide $\mathbf{r}_0=(0,0,0)$, with intensity proportional to $G(\mathbf{r}|\mathbf{r}_0)G^*(\mathbf{r}|\mathbf{r}_0)$, in Fig. 4. The intensity structure is only similar for the 50-Hz case where $ka\approx2$, and monopolelike behavior is anticipated in the scattered field intensity.

We next consider the azimuthal coherence of the scattered noise fields $R_{SS}(\rho,\Delta\phi)$, shown in Fig. 5. Note that for a monopole source, the phase fronts will be cylindrically symmetric and $R_{SS}(\rho,\Delta\phi)=1$. However, this is not the case for the scattered noise fields, unless $ka\ll1$. The azimuthal coherence has distinct spatial variations which change with frequency, object size and boundary condition. For the examples shown we find that $R_{SS}(\rho,\Delta\phi)$ falls from near unity at azimuthal separations $\Delta\phi\approx0$ to less than half this value at $\Delta\phi\approx\lambda/(2a)$. This demonstrates that there is an upper bound on the azimuthal coherence scale of the scattered noise. This bound is apparently the ratio of the only two scales available in the scattering, the wavelength of the noise λ, and the diameter of the sphere $2a$. For future reference, we define the azimuthal correlation scale of the scattered noise as $\Delta\phi_c\leq\lambda/(2a)$. The constancy of $\Delta\phi_c$ over increasing range indicates angular spreading. The fact that it is a stationary function of azimuthal separation reflects the azimuthal homogeneity of the noise. In contrast, the azimuthal coherence of a horizontally propagating planewave of wavelength λ varies with horizontal range ρ about a point, and is not stationary. For example, the coherence peak is only about the propagation direction, and it decays to less than half value at an angular increment on the order of $\sqrt{\lambda/\rho}$, when this angle is small enough to be approximately equal to its sine. A physical interpretation for the azimuthal coherence scale, as well as its ramifications upon detection and imaging, is presented in Appendix C.

Finally, we compare the total noise field intensity with

Redistribution subject to ASA license or copyright; see http://acousticalsociety.org/content/terms. Download to IP: 18.38.0.166 On: Mon, 12 Jan 2015 18:30:17

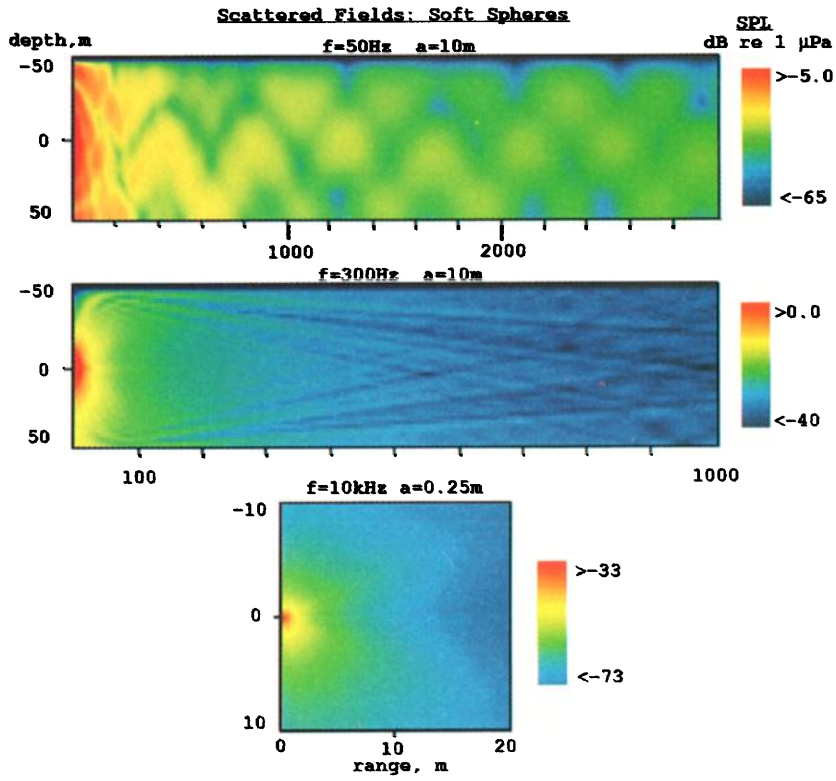

FIG. 3. Scattered noise-field intensity for pressure release spheres centered in the waveguide with $h=100$ m and $d=50$ m for the frequencies shown. Ranges extend from the sphere's center. Sphere radii are as shown. Sound-pressure level is abbreviated by SPL.

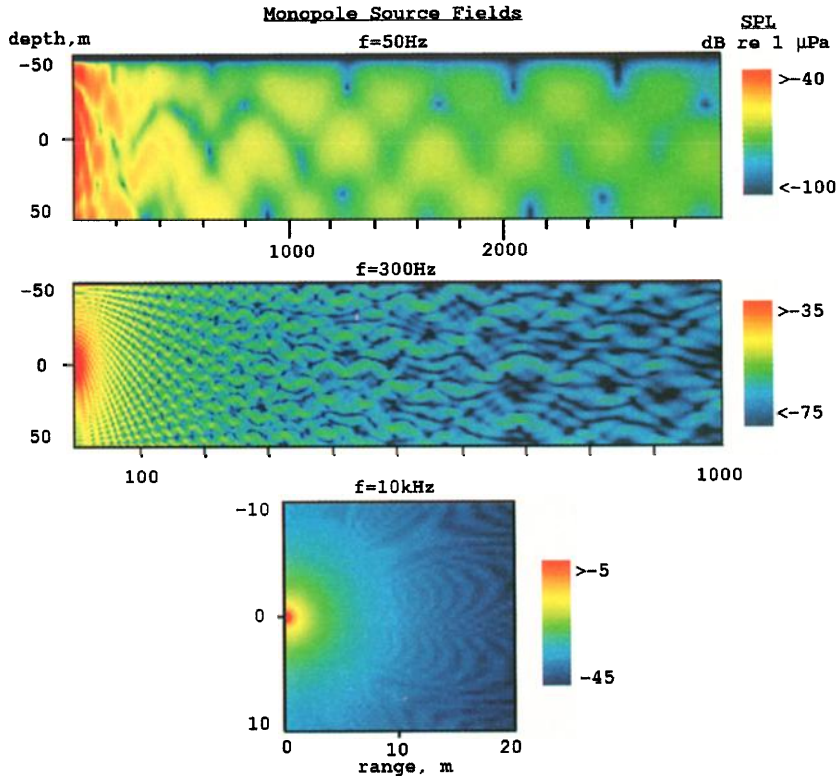

FIG. 4. Monopole source-field intensity for the waveguide and frequencies of Fig. 3. The point source is centered at $d=50$ m for each example.

Redistribution subject to ASA license or copyright; see http://acousticalsociety.org/content/terms. Download to IP: 18.38.0.166 On: Mon, 12 Jan 2015 18:30:17

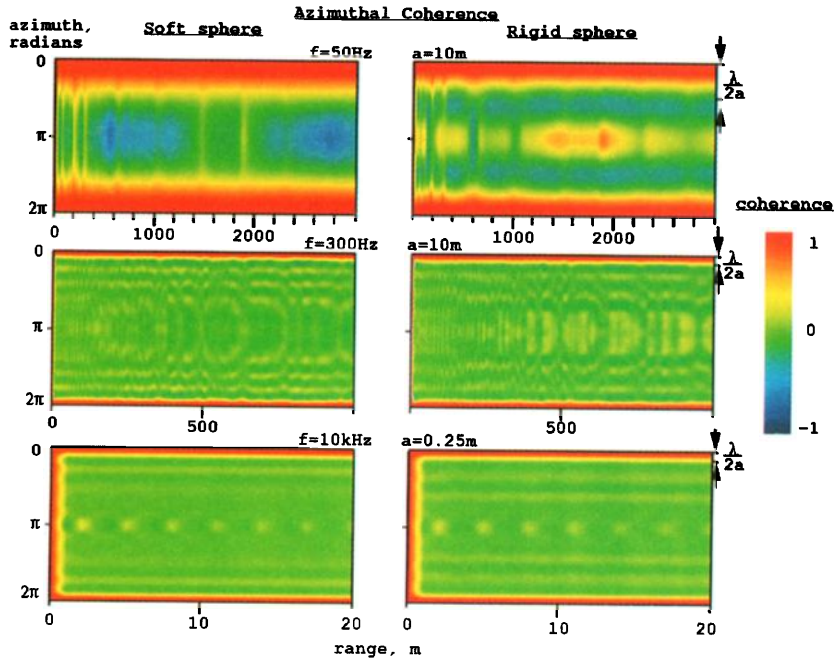

FIG. 5. Azimuthal coherence for a spherical object centered in the waveguide where $h=100$ m and $d=50$ m for the frequencies shown. The coherence is for a horizontal plane passing through the center of the object. Both soft and rigid boundary conditions are shown. Ranges extend from the sphere's center. The azimuthal correlation scale of the scattered noise is limited to within $\lambda/(2a)$.

and without the object present, as is shown in Fig. 6. The total noise field intensity includes the cross terms between the scattered and direct noise field, see Eq. (35). These terms are important since they can be on the order of the scattered field intensity, see Eq. (34), and significantly alter the structure of the total field near the object. For λ/h and a/h approaching unity, the single scatter approximation is not valid at very short ranges. This is evident in Fig. 6 where the field total does not uniformly vanish on the $a=10$-m pressure release spheres at 50 and 300 Hz. For λ/h and a/h small, the single scatter approximation is a good one at very short ranges. This is evident in Fig. 7 where the total field does uniformly vanish on the $a=0.25$-m pressure release sphere at 10 kHz. (Situations in which the cross terms may be significantly diminished are discussed in Appendix D.) For the higher ka cases of $f=300$ Hz and $f=10$ kHz, omnidirectional detection by scattered noise seems to be limited to within the deep shadow range of the object. This range is

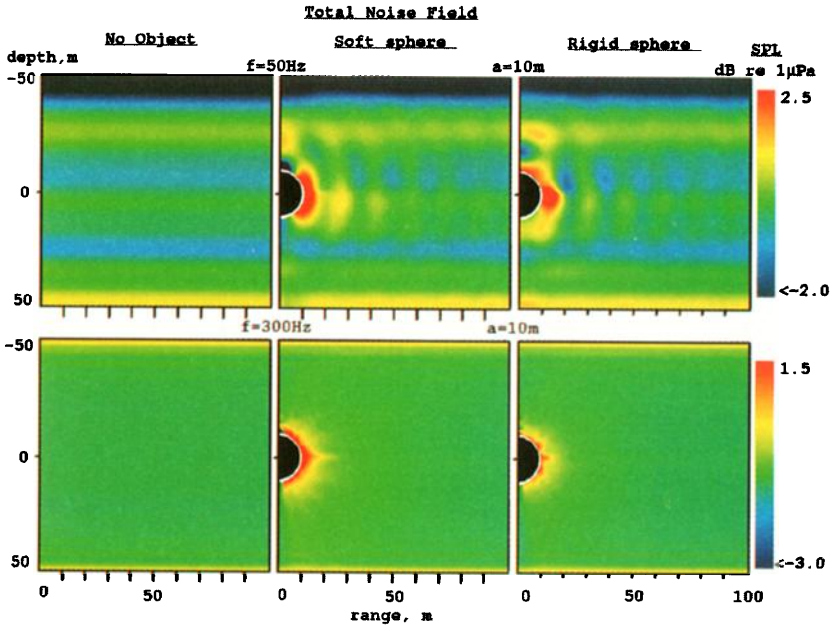

FIG. 6. Total noise-field intensity with and without a spherical object present in the waveguide for $h=100$ m, $d=50$ m. Both 50 and 300 Hz low frequency cases are shown for soft and rigid boundary conditions on the $a=10$-m radius sphere. The sphere is displayed by a black semicircle with white perimeter.

Redistribution subject to ASA license or copyright; see http://acousticalsociety.org/content/terms. Download to IP: 18.38.0.166 On: Mon, 12 Jan 2015 18:30:17

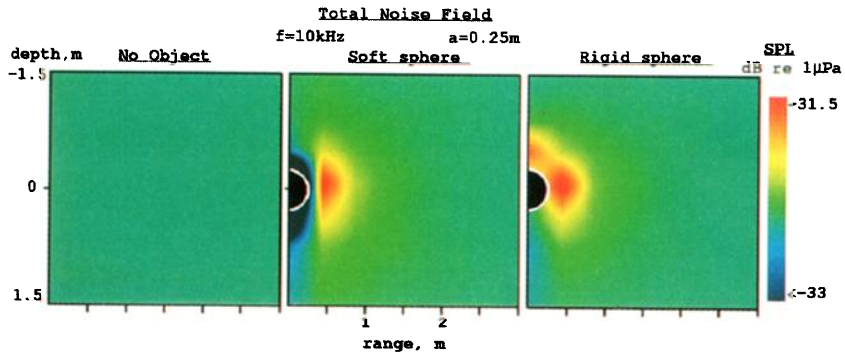

FIG. 7. Total noise-field intensity with and without a spherical object present in the waveguide for high frequency $f=10$ kHz, $h=100$ m, $d=50$ m. Both soft and rigid boundary conditions on the $a=0.25$-m radius sphere are investigated. The sphere is displayed by a black semicircle with white perimeter.

defined in Appendix C for free space conditions. (For the above frequencies this range translates to roughly 18 and 0.43 m, respectively.) For the lower ka and higher λ/h (50 Hz) case, a shadow range is not well defined. Here, omnidirectional detection is evidentially plausible within a water depth in range.

IV. DETECTION

The simulations of the previous section and the analysis of Appendix C indicate that:

(1) Object detection solely by exploitation of scattered surface noise presses the limits of current technology. This is primarily because the SNR is typically near 0 dB in the vicinity of the object and falls off rapidly with increasing range and frequency.

(2) In directions where the incident noise spectrum peaks, and $ka>1$, forward scattering can dominate the scattered noise field. When this occurs, an angular coherence scale of roughly $\lambda/(2a)$ about the object is measured, corresponding to the angular width of the forward scatter peak for a single incident plane wave. Under these conditions, increasing the aperture of a coherent array beyond this coherence scale will not increase the array gain or significantly enhance detection in a measurement of the scattered field; and cross-range resolution will be limited to the scale of the object. The noise directional spectra for the shallow water situations presented peak near the horizontal. This causes the angular coherence scale just described to occur in the azimuthal plane about the object. The azimuthal homogeneity of the noise insures that the coherence scale is stationary in azimuth.

(3) High resolution imaging of reflected ambient noise is most effective within the deep shadow range of the object $a(ka/2)^{1/3}$, defined in Appendix C. Beyond this range diffractive interference from the total forward field may overwhelm reflections, depending upon the incident noise directional spectrum and measurement range. (Increasing object size has a proportionally much greater effect in extending the shadow range than increasing frequency.)

(4) The standard monopole point source field does not provide a good replica for matched field processing, even for a spherical object, unless $ka \ll 1$. Therefore, we avoid matched field processing in this initial investigation. (More sophisticated detection techniques are discussed in the concluding section.)

Instead we provide some examples of detection and imaging of the object by plane-wave beamforming in Sec. IV A. This is for the array specified below and the frequencies previously considered. In Sec. IV B, we address the more general localization issue by presenting the Cramer–Rao bound on resolution of the object in range, cross range, and depth. We use a soft sphere in all cases only because the corresponding detection thresholds are slightly larger.

For our sensor, we use a simple upright billboard array with $N=7\times7$ hydrophones at $\lambda/2$ spacing and length $L=(\sqrt{N}-1)\lambda/2$. The angular resolution is therefore fixed for all examples. The geometry of the array with respect to the object is shown in Fig. 8. The beampattern of the array is shown in Fig. 9. A billboard array has obvious advantages in its ability to reject unwanted noise in three dimensions as well as its ability to maintain relatively large array gain and still fit into a shallow waveguide at low frequency.

A. Coherent imaging

For detection, we use both the standard Bartlett processor

$$P_{\text{Bart}}(\mathbf{a})=\mathbf{A}^{\dagger}(\mathbf{a})\mathbf{C}(\mathbf{a}_0)\mathbf{A}(\mathbf{a}), \tag{38}$$

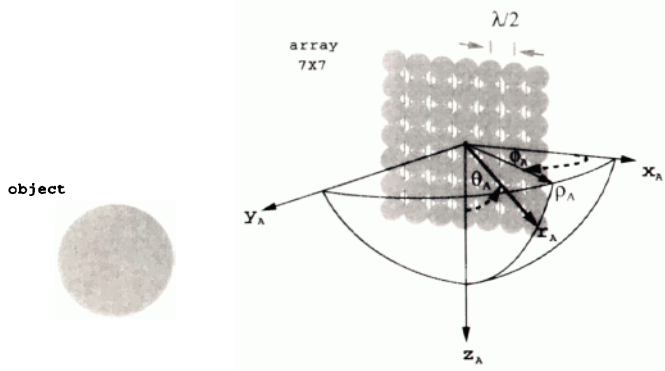

FIG. 8. Detection geometry of the object and sensor are shown. The sensor is a 7×7 element upright billboard array. Individual hydrophones are at $\lambda/2$ spacing. The broadside axis of the array y_A is in the same vertical plane as the sphere's center for all examples in this paper.

Redistribution subject to ASA license or copyright; see http://acousticalsociety.org/content/terms. Download to IP: 18.38.0.166 On: Mon, 12 Jan 2015 18:30:17

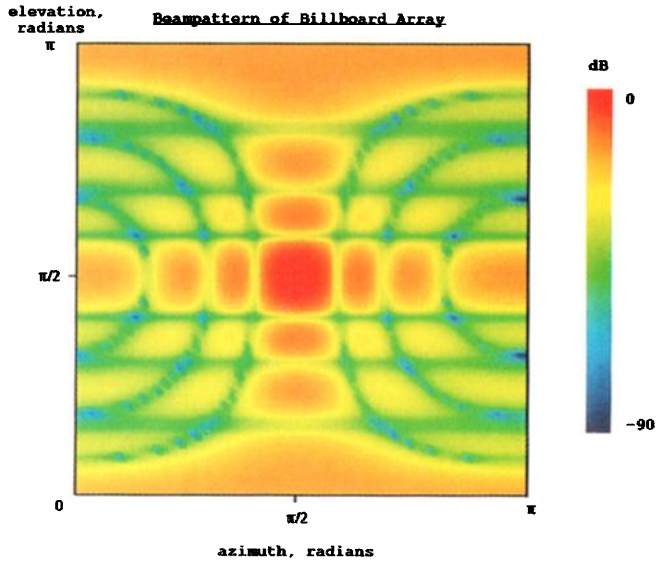

FIG. 9. The normalized beampattern of the billboard array described in Fig. 8 steered to broadside, in the horizontal and vertical. The Rayleigh resolution is $\lambda/L = 19°$. The main lobe occupies twice this angular width. The lobe structure is that for a rectangular taper. Note that the vertical endfire directions are projected onto a line rather than a point due to the coordinate system chosen (azimuth versus elevation angle). The dB reference units are normalized pressure^2/steradian.

and the minimum variance distortionless processor (MVDP) processor, also known as the maximum likelihood method (MLM),[13,14]

$$P_{\mathrm{MVDP}}(\mathbf{a}) = \{\mathbf{A}^{\dagger}(\mathbf{a})\mathbf{C}^{-1}(\mathbf{a}_0)\mathbf{A}(\mathbf{a})\}^{-1}. \tag{39}$$

The normalized replica vector $\mathbf{A}(\mathbf{a})$ contains the synthetic measurements $A_j(\mathbf{a})$ for each sensor $\mathbf{r}_j$. These are evaluated at the search coordinate $\mathbf{a}$. The normalized covariance matrix of the total noise field

$$\mathbf{C}(\mathbf{a}_0) = \frac{C(\mathbf{r}_j, \mathbf{r}_k)}{\Sigma_{j=1}^{N} C(\mathbf{r}_j, \mathbf{r}_j)}, \tag{40}$$

is measured at sensors $\mathbf{r}_j$ and $\mathbf{r}_k$ with elements $C(\mathbf{r}_j, \mathbf{r}_k)$ from Eq (22). The object is at coordinates $\mathbf{a}_0$. For example in plane-wave beamforming, we have

$$A_j(\mathbf{a}) = \frac{1}{N} \exp\{-i\mathbf{k}\cdot(\mathbf{r}_j - \mathbf{r}_{\mathrm{ref}})\}, \tag{41}$$

where $\mathbf{r}_{\mathrm{ref}}$ is the location of a reference sensor on the array. Since the object is sometimes within the Fresnel zone of the array, see Appendix C, we consider azimuthally focused plane-wave beamforming. In terms of the array coordinates in Fig. 8, the replica field focused at broadside and range ρ_A is

$$A_j(\theta_A, \phi_A) = \frac{1}{N} \exp\left[-ik\left(z_{A_j} \cos\theta_A + x_{A_j} \sin\theta_A \cos\phi_A - \frac{x_{A_j}^2}{2\rho_A} \right) \right]. \tag{42}$$

This includes a quadratic correction term in the phase. For measurement ranges $\rho_A < L/2[L/(2\lambda)]^{1/3}$, higher-order corrections to the phase are necessary otherwise the beamformer output will be nearly identical to that of an unfocused array. Whereas, in matched field processing with a point source, the replica field is

$$A_j(\mathbf{a}) = \frac{G(\mathbf{r}_j|\mathbf{a})}{\sqrt{\Sigma_{k=1}^{N} G(\mathbf{r}_k|\mathbf{a}) G^*(\mathbf{r}_k|\mathbf{a})}}. \tag{43}$$

We consider the 50-Hz case first where the vertical aperture of the array nearly spans the full water column; examples are shown in Fig. 10. We begin with the directionality of the noise as determined by the MVDP beamformer. Considering the vertical directionality, two familiar peaks appear about horizontal broadside ($\phi_A = \pi/2$).[14] These are associated with the discrete wavenumber component of the noise field. Steeper angle contributions from direct noise sources above the array and bottom reflections are artificially increased by broadening at endfire in this untapered array. (The coordinate system of the beamformer maps a single direction to a horizontal line in the rectangular directionality plots for both up and down vertical endfire.)

The directionality of the total noise field in the presence of the spherical object at 100-m range also appears in Fig. 10. The MVDP beamformer is used because it significantly outperforms performs the Bartlett processor in these examples. Although the object is in the array's Fresnel zone, including quadratic focus with respect to the object's center has little effect on the measurement and is not included in the example. A noticeable difference in noise directionality occurs over the azimuth of the object. This is distributed in vertical angle due to the waveguide, i.e., the vertical angle of the object cannot be localized by plane-wave beamforming due to boundary interference. A detection level of roughly 1.4 dB is found for an object center at 100-m range, and 0.1 dB at 0.5-km range. Note from the figure caption that detection is significantly enhanced by the presence of cross terms in the 100-m detection. We consider the object dimension to be nominally resolvable by the array when the angle the object subtends is greater than or equal to the λ/L broadside (Rayleigh) resolution. While the object dimension is slightly under-resolved at 100-m range, the example indicates that detection is still plausible. At 0.5-km range, the array's resolution is too poor to resolve the object which has become practically undetectable by beamforming.

We next consider the 300-Hz case, in Fig. 11, for the same object dimension, boundary conditions and ranges shown in Fig. 10. This time the frequency-scaled array occupies 15 m of the water column, and the object is in the far field of the array. Detection thresholds are similar to those in the 50-Hz examples. Detection is not significantly enhanced by the presence of cross terms. This will be discussed further in the next subsection.

Finally, we consider the 10-kHz case for the reduced sphere diameter and much closer ranges, shown in Fig. 12. The array length is now 0.45 m, or roughly the diameter of the object which is in the array's far field. We find a significant 3.6-dB detection level at 2.0-m range from the object center. For this short range, bottom loss is insignificant as is waveguide interference. Therefore, the object is localized in both range and azimuth by plane-wave beamforming. At 2.0

Redistribution subject to ASA license or copyright; see http://acousticalsociety.org/content/terms. Download to IP: 18.38.0.166 On: Mon, 12 Jan 2015 18:30:17

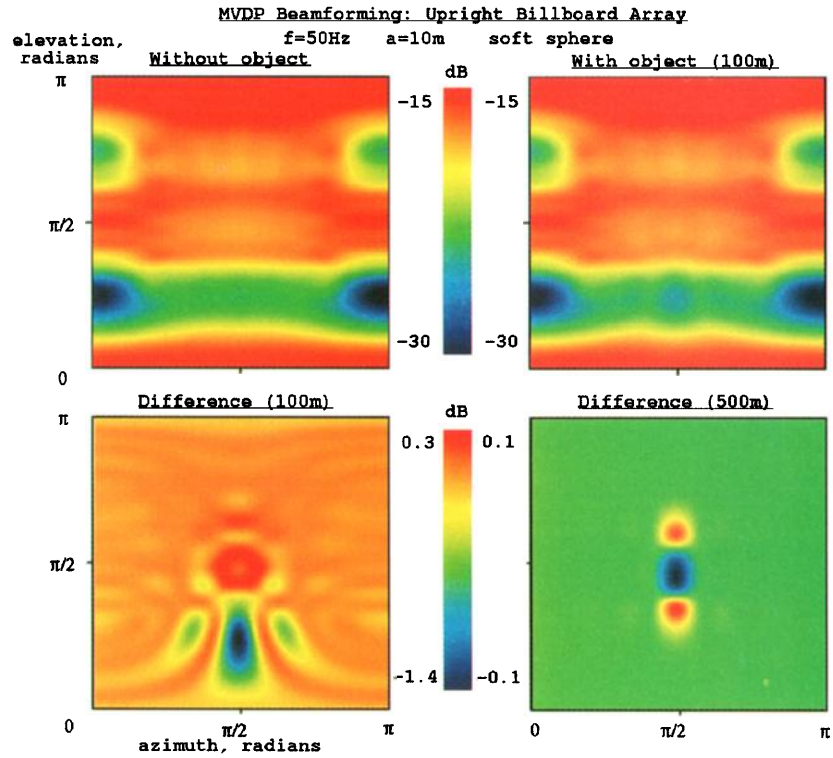

FIG. 10. Directional characteristics of the total noise field over elevation and azimuth angle are shown. These are obtained using unfocused, normalized MVDP beamforming with the billboard array described in Figs. 8–9. The dB reference units are normalized pressure^2/steradian. The upper plots show cases with and without the object present. These are for $f=50$ Hz, $h=100$ m, $d=50$ m, and the array center in the middle of the waveguide. The object's presence is apparent in the beamformer output. In the lower examples, the beamformer outputs with and without the object are differenced in decibels to highlight the detection level. At 100-m range from object center, the detection level is roughly 1.4 dB and at 0.5-km range, it is 0.1 dB. When covariance terms representing the correlation between the direct and scattered noise fields are eliminated, the detection level is reduced to 0.2 dB for 100-m range and 0.05 dB for 0.5-km range.

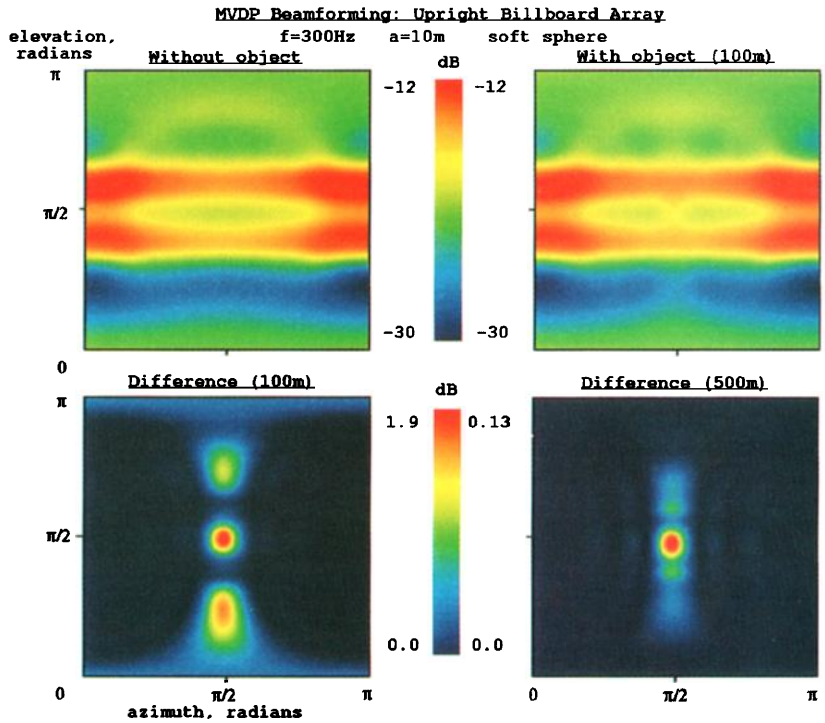

FIG. 11. Same as Fig. 10 except $f=300$ Hz. The object's presence is not apparent in the beamformer output. The object is in the far field of the array. The detection levels are similar to those in the previous, lower frequency, example. When covariance terms representing the correlation between the direct and scattered noise fields are eliminated, the detection level is 1.5 dB for 100-m range and 0.13 dB for 0.5-km range. Their effect is less significant than in the lower frequency example.

Redistribution subject to ASA license or copyright; see http://acousticalsociety.org/content/terms. Download to IP: 18.38.0.166 On: Mon, 12 Jan 2015 18:30:17

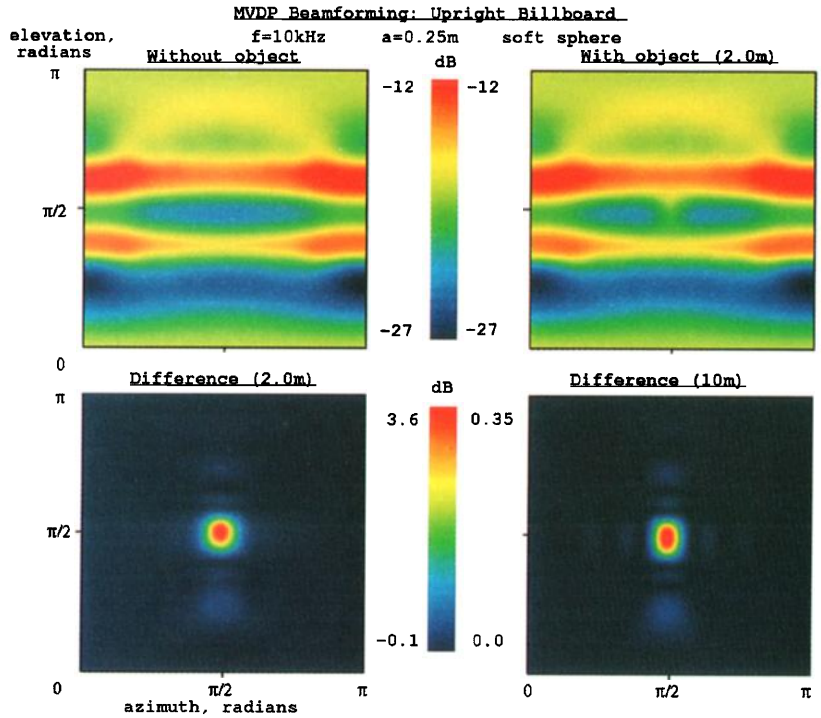

FIG. 12. Same as Fig. 10 except $f=10$ kHz, and the object size and boundary condition have been altered as indicated in the figure. The object is in the far field of the array. The object's presence in the beamformed output is apparent at 2.0-m range from object center. The detection levels show a maximum of roughly 3.6 dB at 2.0 m, and 0.35 dB at 10.0-m range. When covariance terms representing the correlation between the direct and scattered noise fields are eliminated, these levels are unchanged.

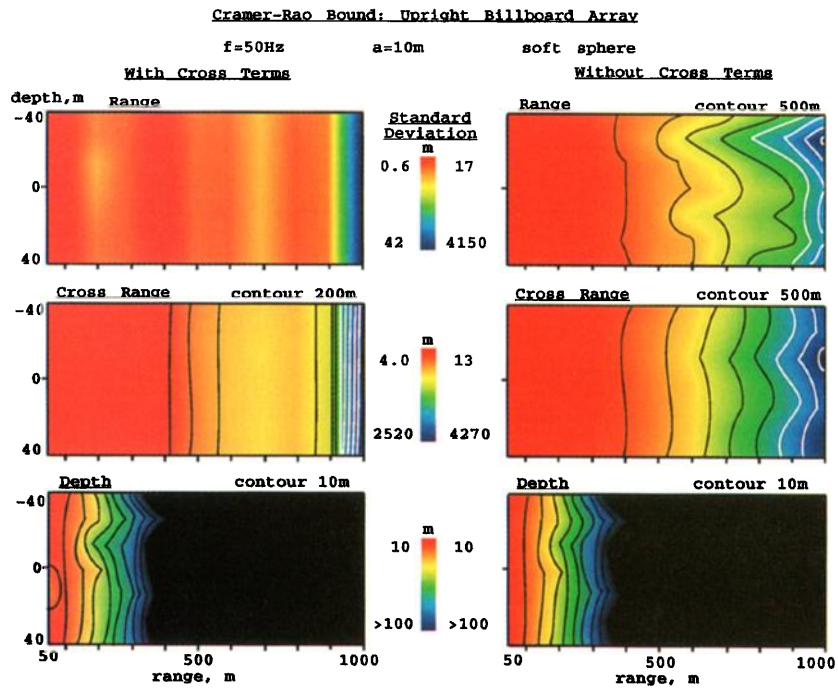

FIG. 13. Cramer–Rao lower bound on detection error for a sphere in a waveguide with $f=50$ Hz, $h=100$ m, $d=50$ m. The bound is computed with and without covariance cross terms included as shown. The sphere center is in the same horizontal plane as array broadside. Only object-center ranges of 50–1000 m and depths of -40 to 40 m with respect to the array center are shown. The array is centered in the middle of the waveguide at $z=0$. The minimum detection error for object range, cross range and depth localization are shown.

Redistribution subject to ASA license or copyright; see http://acousticalsociety.org/content/terms. Download to IP: 18.38.0.166 On: Mon, 12 Jan 2015 18:30:17

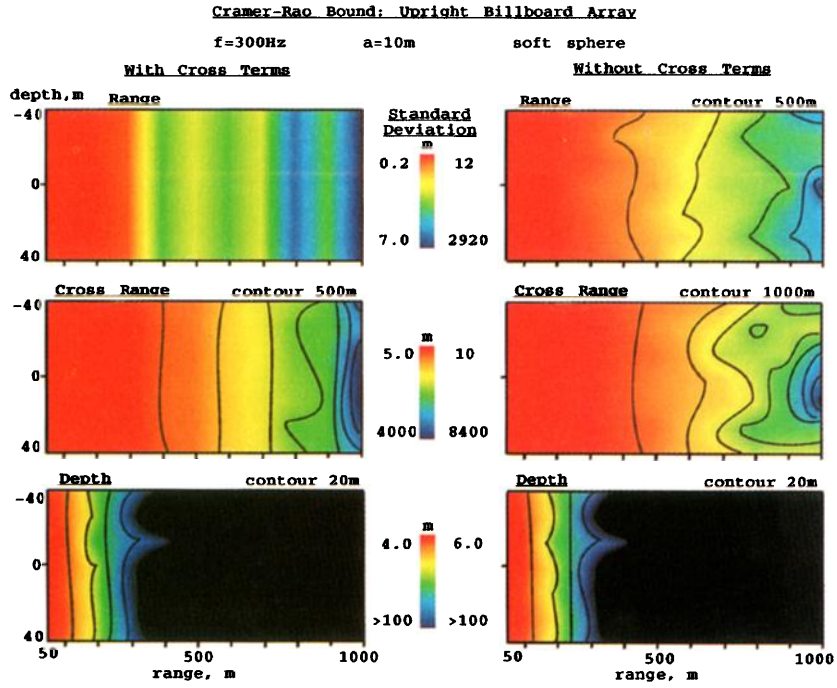

FIG. 14. Same as Fig. 13 except $f=300$ Hz.

m, the object dimension is resolvable by the array. However, at 10.0-m range, the object dimension is no longer resolvable and detection is questionable. The effect of cross terms is again far less significant at higher frequency. In general, this example is not inconsistent with the high frequency–short range experimental results of Ref. 3 discussed in the Introduction. Further, both the array aperture and broadside resolution are roughly the same as the respective aperture and resolution of a dolphin's receiving sonar at 10 kHz.[15] Evidentially, small objects such as prey may be passively detectable by dolphins simply from their scattered noise fields at high frequency.

It is noteworthy that beyond the deep shadow range, the 10-kHz scattered-field intensity of Fig. 3 can now be easily

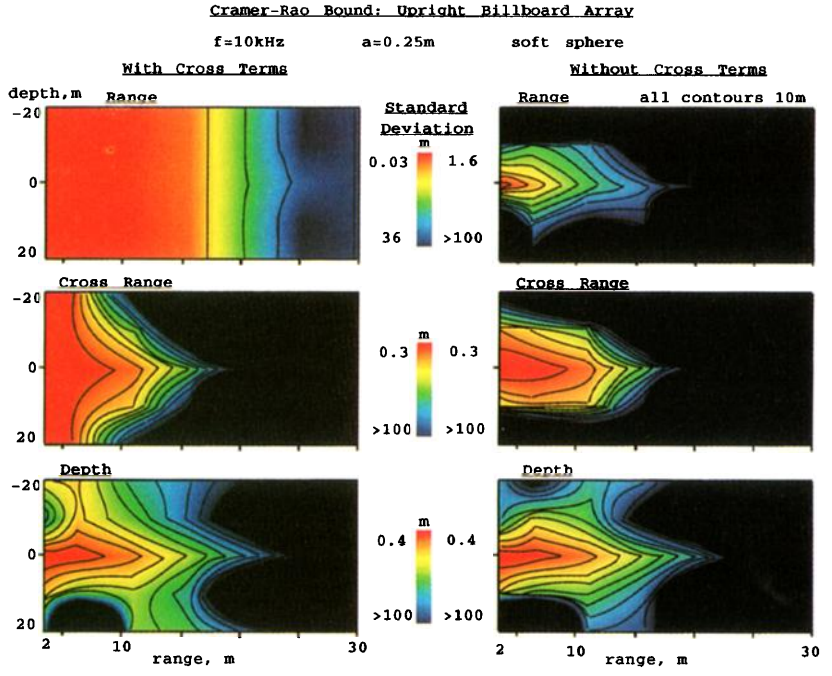

FIG. 15. Same as Fig. 13 except $f=10$ kHz; sphere dimension and boundary conditions are as indicated in the figure; and only object-array ranges of 2.0–30.0 m and depths of -20 to 20 m are shown.

Redistribution subject to ASA license or copyright; see http://acousticalsociety.org/content/terms. Download to IP: 18.38.0.166 On: Mon, 12 Jan 2015 18:30:17

interpreted in terms of forward scatter of the incident noise directional spectrum shown in Fig. 12.

B. Cramer–Rao bounds

We use the Cramer–Rao upper bound on performance to determine conditions in which an object may be detected by scattered surface noise. The bound gives the optimal resolution obtainable for the given sensor, environmental conditions and parameters to be estimated according to estimation and detection theory.[16] We compute the bound on range, cross-range and depth resolution of the object for the shallow water scenarios presented in previous examples. We begin with Eq. (32) of Ref. 14 which describes the lower bound on the mean-square estimation error for any unbiased estimator as

$$E[(\hat{a}_i - a_i)^2] \geqslant [\mathbf{J}^{-1}]_{ii}, \tag{44a}$$

where elements of the Fisher information matrix are given by

$$J_{ij} = \mathbf{Tr}\left(\mathbf{C}^{-1}(\mathbf{a}) \frac{\partial \mathbf{C}(\mathbf{a})}{\partial a_i} \mathbf{C}^{-1}(\mathbf{a}) \frac{\partial \mathbf{C}(\mathbf{a})}{\partial a_j} \right), \tag{44b}$$

and $\hat{\mathbf{a}}$ is the estimated position, while $\mathbf{a}$ is the actual position. This expression is valid under the assumption that harmonic components of the noise can be characterized by a second moment, or Gaussian probability distribution.

In all of the examples presented, in Figs. 13–15, the same $\lambda/2$ spaced $N=7\times7$ element upright billboard array is again placed in the center of the waveguide, and oriented with its broadside axis horizontal and in the vertical plane passing through the object center. The object is then moved within this plane in depth and range from the array. A plot of the Cramer–Rao lower bound for these respective object locations is then given on object range, cross range, and depth estimation error. This is done by numerically computing the square root of the mean square estimation error given in Eq. (44a), where the covariances are again determined by numerical wave number integration. To show how correlation between the direct and scattered noise field enhances detection, a separate plot is given for the root mean-square estimation error with and without these covariance cross terms included.

Considering the 50-Hz case first, a dramatic reduction in minimum detection error is found in range and cross range when cross terms can be included. Also, when these bounds are related to the previous beamforming examples, it is clear that the MVDP beamformer's performance in cross range and depth resolution is near optimal. Therefore, seeking a better detection method for these parameters would not be necessary. Also, it is clear that the object can only be effectively localized in cross range and depth when the angle it subtends is resolvable by the array. This is observed in the previous beamforming examples. On the other hand, high resolution localization in range is plausible out to 1.0 km. A modified MFP technique may meet this bound, as discussed in the concluding section.

At 300 Hz, the bounds are similar to those found in the 50-Hz case. For example, cross-range localization is most effective when the object dimension is resolvable by the array. However, beyond these relatively short ranges, the upper bound on cross-range resolution decreases more rapidly for the higher frequency case. This is apparently due to the more rapid decrease in SNR at higher frequency noted in previous sections. For both 50- and 300-Hz cases, when cross terms are included, localization in range consistently has the least minimum error. This is because the coherent structure of the total field is most sensitive to object perturbations in range.

Finally, we consider the 10-kHz case, which uses a sphere of significantly reduced radius. The bounds on cross range and depth again indicate that localization is only plausible when the object dimension is resolvable by the array. Cross terms only enhance detection for these two parameters when the array is almost directly above and below the object. (In this case, the detection is near endfire where front–back ambiguity on the array is minimized, but so is resolution.) Apparently, for these short-range orientations, perturbations in object cross range and depth have as significant an effect on the field as perturbations in range.

V. SUMMARY AND DISCUSSION

We have investigated the possibility of detecting a submerged object by exploiting the way it disturbs an ocean waveguide's naturally occurring surface-generated noise field. Our approach in this paper is to formulate the problem in terms of wave and scattering theory using a stochastic model for the noise sources. Expressions for the total noise field covariance are derived for an arbitrary object in a stratified ocean waveguide. Specific expressions are derived for a spherical object and evaluated numerically for a shallow water Pekeris waveguide. The only simplifying assumption is that multiple scattering between the object and the waveguide boundaries can be neglected. Detections are simulated using a conventional upright billboard array design, with 7×7 elements at $\lambda/2$ spacing.

We have used the Cramer–Rao upper bound on resolution to determine some conditions in which an object may be detected by scattered surface noise for several realistic shallow water scenarios. The results indicate that (1) cross-range localization is possible when the array aperture is sufficient to resolve the object scale. This is supported by minimum-variance beamforming simulations. Over ranges great enough for bottom interaction to significantly affect transmission of scattered noise, lower frequency detections may be favored due to higher SNR. (2) Range localization is possible at greater distances. However, this requires high correlation between direct and scattered noise fields at the sensor, which is difficult to replicate via matched field processing which typically neglects correlation between signal and noise. (3) A simple monopole source replica is a poor match for the scattered field unless $ka \ll 1$. A forward scattered wave may prove a more useful replica. Since the scattered noise field is a stochastic quantity, we believe that matched field processing will be of limited value in meeting the Cramer–Rao bound. It is possible that a matched covariance processor may prove to be more optimal, especially if the replica is obtained by full-wave modeling of the total noise covariance, as initial results along these lines suggest.[17]

Redistribution subject to ASA license or copyright; see http://acousticalsociety.org/content/terms. Download to IP: 18.38.0.166 On: Mon, 12 Jan 2015 18:30:17

We have also found that in directions where the incident noise spectrum peaks, and $ka>1$, forward scattering can dominate the scattered noise field. When this occurs, an angular coherence scale of roughly $\lambda/(2a)$ is measured about the object, corresponding to the angular width of the forward scatter peak for a single incident plane wave. Under these conditions, increasing the aperture of a coherent array beyond this coherence scale will not increase the array gain or significantly enhance detection in a measurement of the scattered field. These conditions also limit cross-range resolution to the scale of the object regardless of sensor aperture. For the shallow water scenarios presented here, the noise directional spectra peak near the horizontal. This causes the angular coherence scale just described to occur in the azimuthal plane about the object. The azimuthal homogeneity of the noise insures that the coherence scale is stationary in azimuth.

We find that high resolution imaging of reflected ambient noise is most effective within the deep shadow range of the object $a(ka/2)^{1/3}$. Here the total forward field will cause the least diffractive interference in imaging reflections. Beyond this range, the measurement is most likely to succeed from an orientation such that the incident noise directional spectrum does not peak into the steering direction of the sensor. Otherwise the total forward field may overwhelm reflections. However, maintaining such an orientation is difficult for imaging ranges greater than a water depth. This is because the directional spectrum of shallow-water noise tends to peak about the horizontal. For example, we find that including diffraction from the object may substantially alter the simulated images of Ref. 18. These were obtained by raytrace assuming specular reflection which implies an infinite deep shadow range. In this reference, imaging is simulated for a sensor at 20 m from a 1-m radius sphere at 75 kHz. However, our analysis indicates that deep shadow ends at 5 m. A 20-m measurement is in the range of the Poisson diffraction cone where the total forward field intensity due to an incident plane wave is on the order of the incident field. (The specific situation is discussed in more detail in Appendix C, where it is shown that the total forward field overwhelms reflections for incident plane waves of equal incident intensity.) Since 75 kHz is near the upper frequency limit of propagating noise in the ocean,[3] this result indicates that wave theory is generally necessary to properly model acoustic imaging with ambient noise in the ocean. A useful optical analogy might be the theory for imaging extended non-self-luminous objects with incoherent, coherent and partially coherent light.[19] It is noteworthy that wave interference and diffraction caused by the object is an essential element of this classic optical theory.

In summary, the detection scheme proposed in the title of this paper presses the limits of current technology for azimuthally homogeneous noise. Recent work[8] indicates that an azimuthally directional noise field, such as a coastline where surf is generated, can provide a natural means of separating direct and scattered noise to increase the detection threshold. In this case, it may no longer be necessary to have aperture sufficient to resolve the scale of the object. Simple but robust methods such as beamforming could be practical at relatively long ranges. Detections would also be less sensitive to environmental fluctuations.

Finally, we note that the array aperture and resolution of our high frequency examples are roughly the same as those of a dolphin's sonar, operating in the 10-kHz range.[15] These examples show that a dolphin may be able to detect small objects, such as prey, within a few meters range simply by the object's disruption of the noise field. The Cramer–Rao bound suggests that this is not possible at much greater ranges for the given frequency. The dolphin's evolutionary adaptation of active insonification is consistent with this result.

DEDICATION

The first author would like to thank his brother for past conversations which motivated this work. One of these was their last. Dr. John C. Makris (1960–1992) was killed in the North Pacific during the early part of this research. "*...All those moments will be lost in time like tears in rain...* ."

ACKNOWLEDGMENTS

We thank our colleagues at NRL Dalcio Dacol and John Perkins for many useful discussions.

APPENDIX A: DERIVATION OF THE SCATTERED NOISE FIELD COVARIANCE FOR A SPHERE IN A WAVEGUIDE

We begin by introducing the plane-wave scatter function for a sphere

$$S(\alpha,\beta;\alpha_i,\beta_i)=S(\eta(\alpha,\beta;\alpha_i,\beta_i)) = \sum_{n=0}^{\infty} f(n)P_n(\eta(\alpha,\beta;\alpha_i,\beta_i)). \tag{A1}$$

Rewriting the cosine of the incidence angle in terms of the vertical wave number we have

$$S(\alpha,\beta;\alpha_i,\beta_i)=S\left(\frac{1}{k^2}[\gamma\gamma_i+\xi\xi_i\cos(\beta-\beta_i)]\right) = \sum_{n=0}^{\infty} f(n)\left[P_n\left(\frac{\gamma}{k}\right)P_n\left(\frac{\gamma_i}{k}\right) + 2\sum_{m=1}^{n}\frac{(n-m)!}{(n+m)!}P_n^m\left(\frac{\gamma}{k}\right) \times P_n^m\left(\frac{\gamma_i}{k}\right)\cos m(\beta-\beta_i)\right], \tag{A2}$$

where we have used the addition theorem for spherical harmonics. We then rewrite Eq. (28) as

Redistribution subject to ASA license or copyright; see http://acousticalsociety.org/content/terms. Download to IP: 18.38.0.166 On: Mon, 12 Jan 2015 18:30:17

$$C_{SS}(\mathbf{r},\mathbf{r}')=(2\pi)^3\left(\frac{2q^2}{k^2}\right)\left(\frac{1}{\pi k}\right)^2\int_0^{\infty}\int\int d\xi_i\, d\xi\, d\xi'\ \xi_i\xi\xi'\{\Delta(z,z_0;\xi,\xi_i)\Delta^*(z',z_0;\xi',\xi_i)\Xi^{++}$$
$$+\Delta(z,z_0;\xi,\xi_i)\Gamma^*(z',z_0;\xi',\xi_i)\Xi^{+-}+\Gamma(z,z_0;\xi,\xi_i)\Delta^*(z',z_0;\xi',\xi_i)\Xi^{-+}$$
$$+\Gamma(z,z_0;\xi,\xi_i)\Gamma^*(z',z_0;\xi',\xi_i)\Xi^{--}\}, \tag{A3}$$

where

$$\Delta(z,z_0;\xi,\xi_i)=[A(z_0)C(z)+B(z_0)D(z)], \tag{A4a}$$

$$\Gamma(z,z_0;\xi,\xi_i)=[A(z_0)D(z)+B(z_0)C(z)], \tag{A4b}$$

and

$$\Xi^{\pm\pm}=\int_0^{2\pi}\int\int d\beta_i\, d\beta\, d\beta'\{e^{i[\xi\cdot\rho-\xi'\cdot\rho']}$$
$$\times S((1/k^2)[\pm\gamma\gamma_i+\xi\xi_i\cos(\beta-\beta_i)])$$
$$\times S^*((1/k^2)[\pm\gamma'\gamma_i+\xi'\xi_i\cos(\beta'-\beta_i)])\}. \tag{A5}$$

This last expression can be simplified to the following:

$$\Xi^{\pm\pm}=(2\pi)^3\sum_{n=0}^{\infty}\sum_{l=0}^{\infty}f(n)f^*(l)\Bigg[J_0(\rho\xi)P_n\left(\pm\frac{\gamma}{k}\right)$$
$$\times P_n\left(\frac{\gamma_i}{k}\right)J_0(\rho'\xi')P_l^*\left(\pm\frac{\gamma'}{k}\right)P_l^*\left(\frac{\gamma_i}{k}\right)$$
$$+2\sum_{m=1}^{\min(n,l)}\frac{(n-m)!}{(n+m)!}\frac{(l-m)!}{(l+m)!}\cos m(\phi-\phi_i)$$
$$\times J_m(\rho\xi)P_n^m\left(\pm\frac{\gamma}{k}\right)P_n^m\left(\frac{\gamma_i}{k}\right)$$
$$\times J_m(\rho'\xi')P_l^{m*}\left(\pm\frac{\gamma'}{k}\right)P_l^{m*}\left(\frac{\gamma_i}{k}\right)\Bigg]. \tag{A6}$$

After substitution into Eq. (A3) and some algebraic manipulation, the various terms can be separated into the sums and products of one-dimensional wave number integrals shown in Eq. (34). After a similar process the same can be done for Eq. (35).

APPENDIX B: AZIMUTHAL COHERENCE

The azimuthal coherence can be defined by a real, normalized, correlation function

$$R_{ss}(\rho;\phi,\phi_1)=\frac{C_{SS}(\rho,z_1,\phi;\rho,z_1,\phi_1)}{\sqrt{C_{SS}(\rho,z_1,\phi_1;\rho,z_1,\phi_1)C_{SS}(\rho,z_1,\phi;\rho,z_1,\phi)}}. \tag{B1}$$

To exploit the cylindrical symmetry of the scattered field intensity and maintain a real value, the azimuthal coherence function must be confined to a horizontal plane. For illustrative examples in this paper, the plane is taken through the middle of the object and waveguide at $z_1=0$.

To understand why the azimuthal coherence can be expressed by a real function, it is instructive to consider Eqs. (34)–(35). The covariance functions $C_{SS}(\mathbf{r},\mathbf{r}')$ and $C_{SN}(\mathbf{r},\mathbf{r}')$, respectively are decomposed into an azimuthally omnidirectional and directional set of terms. This is a consequence of the addition theorem for spherical harmonics. Azimuthal variations in spatial coherence are determined by the $\cos m(\phi-\phi')$ factor in Eqs. (34)–(35), where m determines the order of the spherical harmonics. Therefore, for observations points $\mathbf{r}=(\rho,z,\phi)$ and $\mathbf{r}'=(\rho,z,\phi')$ at the same range and depth, but differing azimuth, the covariance of the scattered field $C_{SS}(\phi-\phi')$ is a real number dependent only upon the azimuthal separation, as is $C_{SN}(\phi-\phi')+C_{NS}(\phi-\phi')$. Since the intensity at a given range is also constant, the azimuthal coherence is a stationary function of azimuthal separation $R_{ss}(\rho;\phi,\phi_1)=R_{ss}(\rho;\Delta\phi)$ where $\Delta\phi=|\phi-\phi_1|$. This is related to the horizontal homogeneity of the noise which also leads the direct noise field covariance to be a real function dependent only upon receiver separation for sensors at the same depth.

APPENDIX C: ARRAY DESIGN AND IMAGING LIMITATIONS IMPOSED BY DIFFRACTION

We find that diffractive interference will generally impose limitations on the ability to image an object by reflected ambient noise in the ocean, even at the high frequency limit suggested in Ref. 3. To demonstrate this, we begin with the geometry and coordinates of a planewave incident upon a perfectly reflecting sphere in Fig. C1. The incident wave propagates in the $\phi_i=180°$ direction. Various regions about the sphere are identified in this adaptation of a diagram from Ref. 9. Specular reflection and the limit of geometric rays is a good approximation in the lit region beyond the Fraunhofer range of the object, see Fig. C2. For shorter ranges, higher order corrections become appropriate.[9] An exact expression for the incident field in the direction ϕ_i and measured at (ρ,ϕ) is given by

$$V^i=e^{ik\rho\cos(\phi-\phi_i)}$$
$$=\sum_{n=0}^{\infty}i^n(2n+1)j_n(k\rho)P_n(\cos(\phi-\phi_i)). \tag{C1}$$

The scattered field measured at (ρ,ϕ) is given by

Redistribution subject to ASA license or copyright; see http://acousticalsociety.org/content/terms. Download to IP: 18.38.0.166 On: Mon, 12 Jan 2015 18:30:17

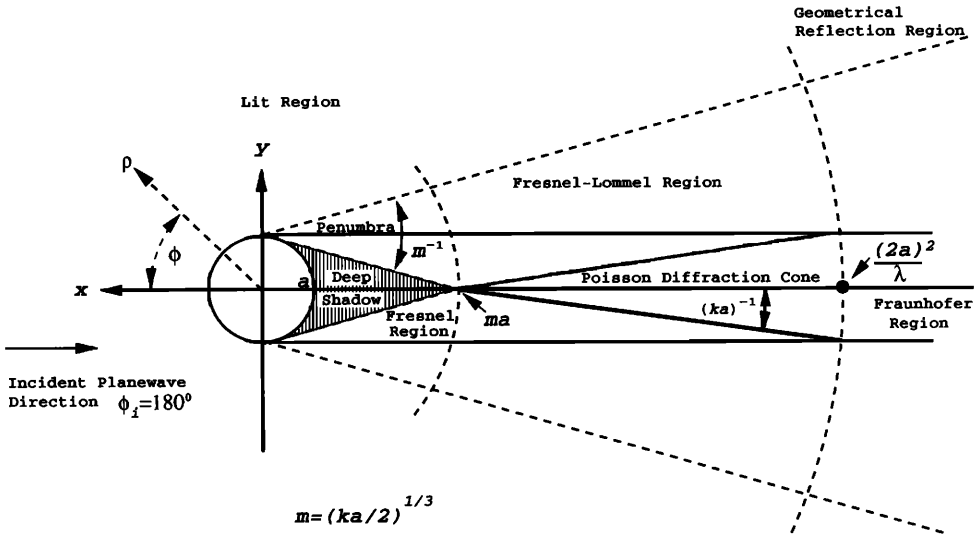

FIG. C1. The geometry and coordinates of a plane wave incident upon a perfectly reflecting sphere. The wave is incident from the $\varphi=0$ direction. Various regions about the sphere are identified in this adaptation of a diagram from Ref. 9.

$$V^s=-\sum_{n=0}^{\infty} i^n(2n+1)a_n h_n^{(1)}(k\rho)P_n(\cos(\phi-\phi_i)), \quad \text{(C2)}$$

where $a_n=j_n(ka)/h_n^{(1)}(ka)$ for a pressure release sphere of radius a, and the outward going spherical Hankel function is used. This is replaced by $a_n' = j_n'(ka)/h_n^{(1)'}(ka)$ for a rigid sphere.

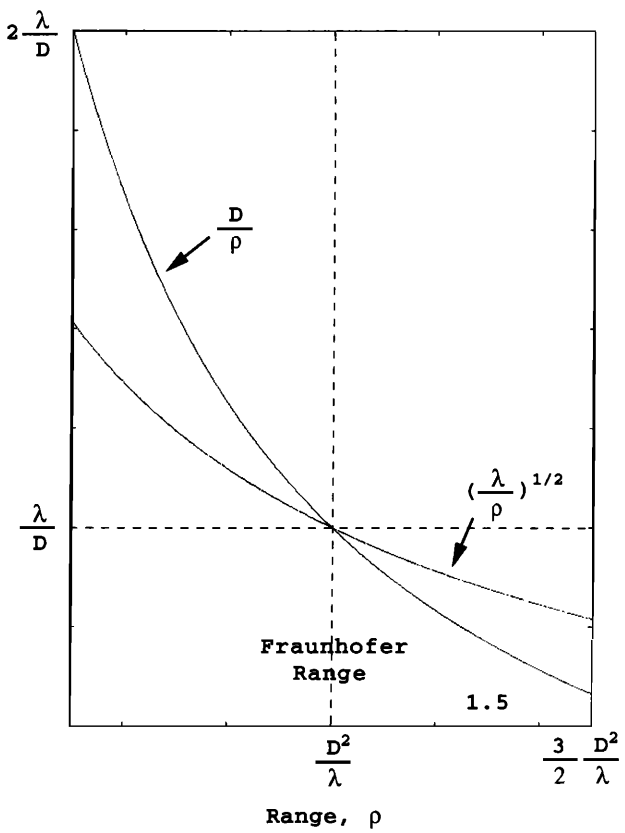

FIG. C2. Graphical interpretation of the Fraunhofer condition. The angle D/r subtended by an object or array of length D from a distance ρ, where $\rho \gg D$. For a point source at ρ from the center of a broadside array, half the aperture must be at least $\rho\sqrt{\lambda/\rho}$ to produce a path length difference greater than $\lambda/4$ between ρ and the range from the source to the end of the array for $\rho \gg \lambda$.

The amplitude and phase of the free-space scattering function S [Eq. (A1)] can be derived from these expressions.[9] These are plotted in Fig. C3 for the $ka \approx 10.5$ of the 10-kHz examples and a soft sphere. The peak of the scattering function is in the forward direction. This decays to less than half amplitude over an angular increment of roughly $\lambda/(2a)$. The angular width of the forward scatter peak roughly maintains this scale well into the Fresnel region of the object. It is no coincidence that this is also the azimuthal coherence scale of the scattered noise found in the waveguide examples of Fig. 5. For example, in directions where the incident noise spectrum peaks, and $ka>1$, forward scattering can dominate the scattered noise field. This leads to an angular coherence scale of roughly $\lambda/(2a)$ about the object, corresponding to the angular width of the forward scatter peak for a single incident plane wave. For the shallow water scenarios presented, the noise directional spectra peak near the horizontal. This causes the angular coherence scale just described to occur in the azimuthal plane about the object. The azimuthal homogeneity of the noise insures that the coherence scale is stationary in azimuth.

In coherent detection, it is desirable to have a coherent signal over the aperture of the sensing array. For example, given N sensors at separations greater than or equal to the horizontal correlation length of the direct noise field $\lambda/2$, the coherent signal is elevated with respect to the noise by the array gain $10 \log N$. Apertures in excess of the signal's coherence length scale are not useful for detection since the incoherent part of the signal will be averaged out with the noise. Therefore, the azimuthal coherence scale $\Delta\phi_c \leq \lambda/(2a)$ sets an upper limit on the useful horizontal aperture for detection by scattered noise at roughly $L_{\max} \leq \rho\Delta\phi_c$, where ρ is range from sensor to object. Similarly, the optimal azimuthal resolution of the object is limited

Redistribution subject to ASA license or copyright; see http://acousticalsociety.org/content/terms. Download to IP: 18.38.0.166 On: Mon, 12 Jan 2015 18:30:17

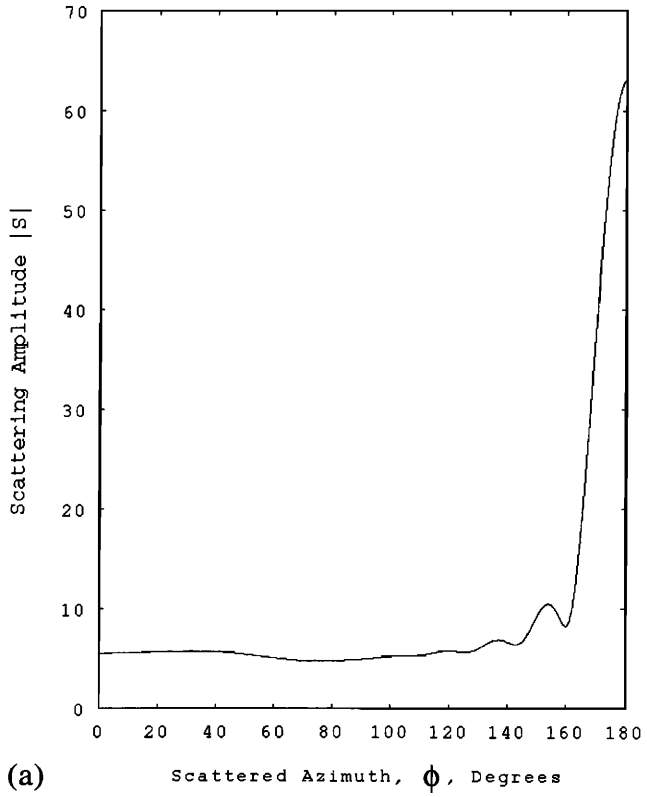

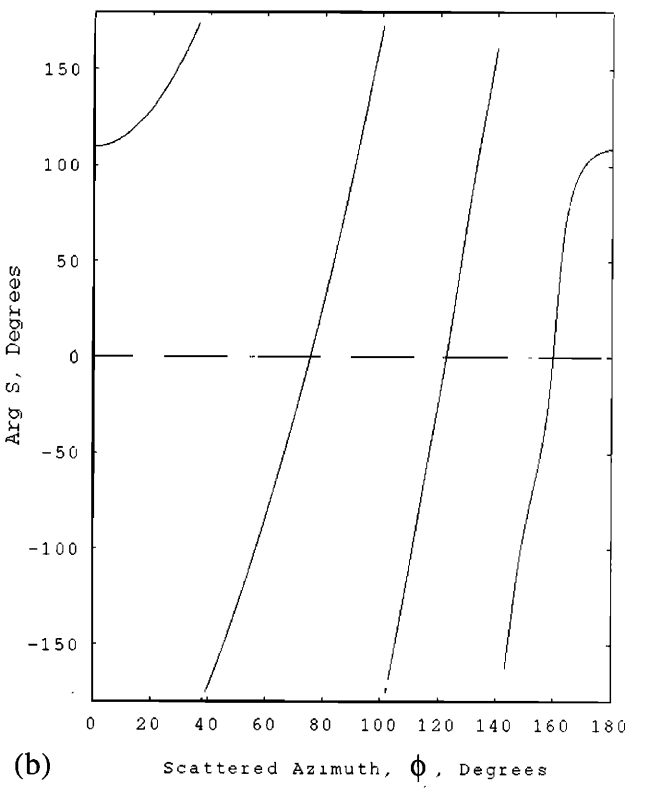

FIG. C3. The magnitude (a) and phase (b) of the free-space plane wave scattering function $S(\theta=0°, \varphi; \theta_i=0°, \varphi_i=180°)$ for $ka \approx 10.5$ and a pressure release sphere. The forward scatter peak is at $\varphi=180°$. This peak decays to half amplitude over an angular width of roughly $\lambda/(2a)$. The slope of the phase is on the order of $2(ka)^{-1}$ for φ near 90°.

by the Rayleigh resolution $\lambda/L_{\max}=\lambda/(\rho\Delta\phi_c)=2a/\rho$ to occupy the angular scale subtended by the object. Under these conditions, increasing the aperture of a coherent array beyond this coherence scale will not increase the array gain or significantly enhance detection in a measurement of the scattered field. These conditions also limit resolution to the scale of the object regardless of sensor aperture.

The implication of these results upon imaging may be interpreted in terms of diffraction by considering the total forward field. Figure C1 also shows that a diffraction cone of intensity comparable to that of the incident field will form in the total field beyond the deep shadow. Therefore, given a receiver beyond the deep shadow range of the object, the total field from a plane wave propagating in the forward direction to the receiver will dominate the field of a reflected planewave because the reflected field suffers spreading loss. This is confirmed by the results shown in Fig. C5. Here Eqs. (C1)–(C2) are used to compute the field measured on a line array for the geometry shown in Fig. C4. Figure C5(a) shows the magnitude of the field measured at each sensor. The expected Poisson diffraction pattern from the total forward field is evident. The peak of the Poisson diffraction cone along the $\phi=180°$ axis is on the order of the incident field. The reflected fields from normal and back incidence plane waves are orders of magnitude lower. However, they do not yet follow inverse square spreading. This is found in the Fraunhofer zone of the object where the scattered field intensity in the lit region is equal to the incident plane-wave intensity divided by $4(\rho/a)^2$. Figure C5(b) shows the measured directional spectra obtained by plane-wave beamforming for the same parameters as in Fig. C5(a). The forward field dominates the reflected arrivals by about 20 dB and shows peaks at angles corresponding to the edges of the object where diffraction begins. The central overlap corresponds to propagation along the Poisson cone axis. The reflected arrivals have width greater than the $\lambda/L=0.9°$ broadside resolution of the array because the measurement range is well within the Fraunhofer range of the array and object. The direction of the central peaks in the two reflected arrivals can be associated with specular reflections to the array center. As expected, diffractive interference limits resolution to the scale of the object. In Fig. C5(c) all parameters are unchanged except the array is placed at $\rho=200$ m, at roughly the Fraunhofer range of the array and object. Diffractive interference from the forward field is greater than in the previous example. The resolution of the array is insufficient to distinguish reflected arrivals, which are truly specular. As expected, the intensity ratio between the total forward and specular arrivals is now $4(\rho/a)^2$. (Note the elevated sidelobe levels well beyond the azimuth of the object.) In Fig. C5(d) the array aperture, and number of elements, is increased by a factor of 3 to $N=387$ and replaced at $\rho=20$ m. The main peaks of the measured directional spectra show increased width. Increasing the aperture of the array caused an increase in diverging beams received from the object. Here the array is too close to the object for a simple quadratic focus to be effective, ie quadratic focus gives essentially the same result as plane-wave beamforming [see Eq. (42)]. This demonstrates that an increased aperture without proper focus can lead to poorer

Redistribution subject to ASA license or copyright; see http://acousticalsociety.org/content/terms. Download to IP: 18.38.0.166 On: Mon, 12 Jan 2015 18:30:17

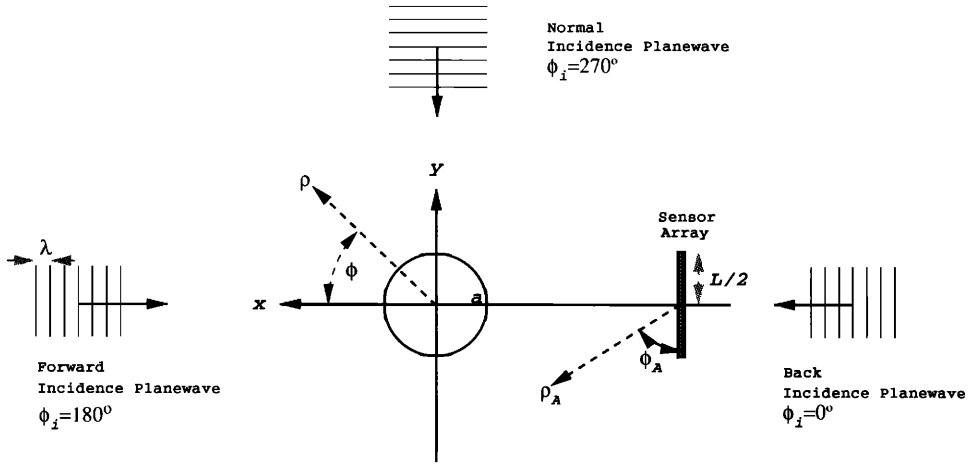

FIG. C4. Three incident plane waves of unit amplitude in μPa are scattered from a rigid sphere and received by a line array beyond the deep shadow range of the object at $\rho > ma$. The array is of length L centered at $\varphi = 180°$ with $\lambda/2$ spacing. The wavelength of $\lambda = 0.02$ m (75 kHz) and sphere radius $a = 1.0$ m are taken from Ref. 18.

resolution. (For example, nearsighted people can often see clearly through a pin hole.) Since the incident forward field in the absence of the object will have measured intensity of 20 log(N) for a unit plane wave, or 42 dB for the examples in Fig. C5(b) and (c), arrivals from the object will appear as a silhouette in comparison. (A simple optical example of this effect is to hold a pen ($a = 5\times10^{-3}$ m) at arms length in front of a dominant light or window ($\lambda = 5\times10^{-7}$ m). The deep shadow ends at roughly $ma = 0.16$ m. Interference from the total forward field dominates specular reflections which are not visible. When the pen is brought to within 0.16 m details of the object due to specular reflections from other sources are visible. However, for a much larger 1-m radius object, the deep shadow ends at a much greater range of 185 m in daylight!)

Because waveguide noise directional spectra are typically confined to two narrow bands about the horizontal (see Sec. IV), the total forward scattered field from the object will dominate reflections in the far field. This is apparent in an incoherent integration of S over azimuth; see Fig. C3. Also, as the resolution of the array increases, arrivals from the object separate in measured direction until the situation shown in Fig. C5(c) occurs. In this limiting case, the total forward field from a single incident plane wave is compared to the reflected field from a single incident plane wave. Here, increasingly large directional variations in incident noise, or object reflectivity, are necessary to overcome diffractive interference at increasing range. Clearly, the measurement orientation must also favor reflected noise at the receiver. The same conclusion can be drawn for an array with a large and fixed number of receiving beams subtending the object.

APPENDIX D: DECORRELATION OF DIRECT AND SCATTERED NOISE FIELDS

We consider two conditions in which the covariance between the direct and scattered noise field may vanish. The first concerns relative motion between sources, scatterer and receiver. The second concerns temporal decorrelation of the noise source signal during travel to the receiver from the scattered and nonscattered paths.

In the former, a scattering object may under go random motion Δr with respect to the sound sources and/or receivers during the sensing time window T. In this case the covariance cross terms $C_{SN}(\mathbf{r},\mathbf{r}')+C_{NS}(\mathbf{r},\mathbf{r}')$ may become negligibly small when relative motion is larger than a wavelength. For example, the expectation value of the cross terms $\langle C_{NS}(\mathbf{r},\mathbf{r}'+\Delta\mathbf{r})\rangle_{\Delta r}$ may vanish. To demonstrate this, in Eq. (35) we replace $I_{CD}(\rho',z';n)$, $I_{DC}(\rho',z';n)$, $\mathfrak{I}_{CD}(\rho', z';n,m)$, and $I_{DC}(\rho',z';n)$ by $\langle I_{CD}(\rho'+\Delta r,z';n)\rangle_{\Delta r}$, $\langle I_{DC}(\rho'+\Delta r,z';n)\rangle_{\Delta r}$, $\langle \mathfrak{I}_{DC}(\rho'+\Delta r,z';n,m)\rangle_{\Delta r}$, and $\langle \mathfrak{I}_{CD}(\rho'+\Delta r,z';n,m)\rangle_{\Delta r}$, respectively, where we have assumed the change in azimuthal angle $\Delta\phi'$ is negligible. Then, for example,

$$\langle \mathfrak{I}_{CD}(\rho+\Delta r,z;n,m)\rangle_{\Delta r} = \int_0^\infty \xi\, d\xi \left[C(z)P_n^m\left(\frac{\gamma}{k}\right) + D(z)P_n^m\left(-\frac{\gamma}{k}\right)\right] \times \langle J_m(\rho\xi+\xi\Delta r)\rangle_{\Delta r}, \tag{D1}$$

where

$$\langle J_m(\rho\xi+\Delta r\xi)\rangle_{\Delta r} \approx \sqrt{\frac{2}{\pi\rho\xi}}\left\langle \cos\left(\rho\xi+\Delta r\xi-\frac{m\pi}{2}-\frac{\pi}{4}\right)\right\rangle_{\Delta r} = \langle\cos(\Delta r\xi)\rangle_{\Delta r} \times \cos\left(\rho\xi-\frac{m\pi}{2}-\frac{\pi}{4}\right)\sqrt{\frac{2}{\pi\rho\xi}} - \langle\sin(\Delta r\xi)\rangle_{\Delta r}\sin\left(\rho\xi-\frac{m\pi}{2}-\frac{\pi}{4}\right) \times \sqrt{\frac{2}{\pi\rho\xi}}. \tag{D2}$$

Redistribution subject to ASA license or copyright; see http://acousticalsociety.org/content/terms. Download to IP: 18.38.0.166 On: Mon, 12 Jan 2015 18:30:17

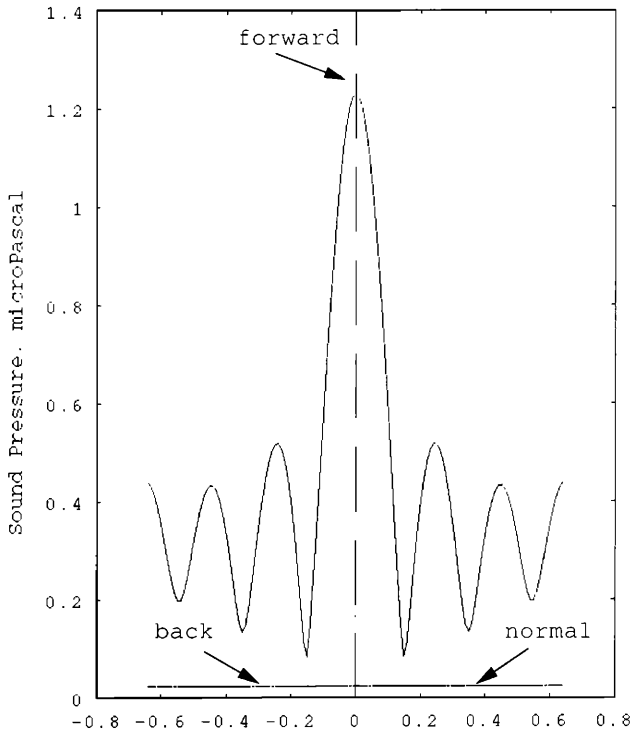

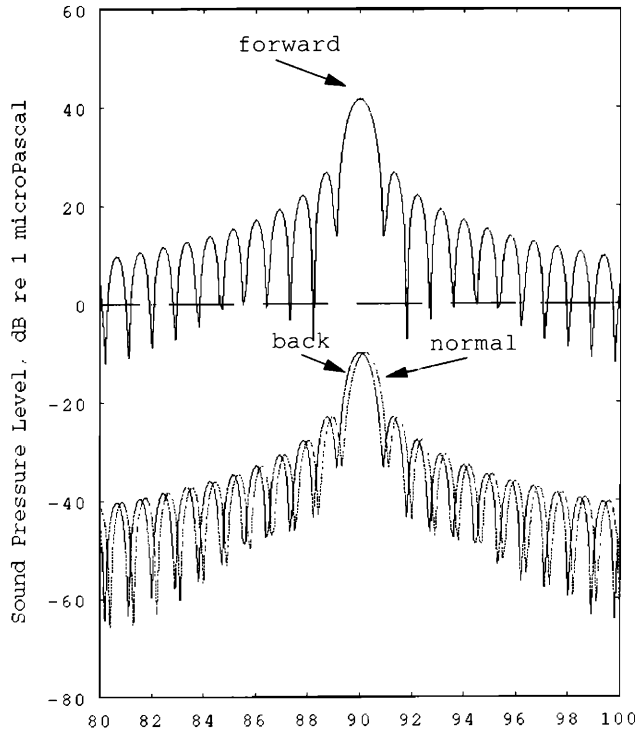

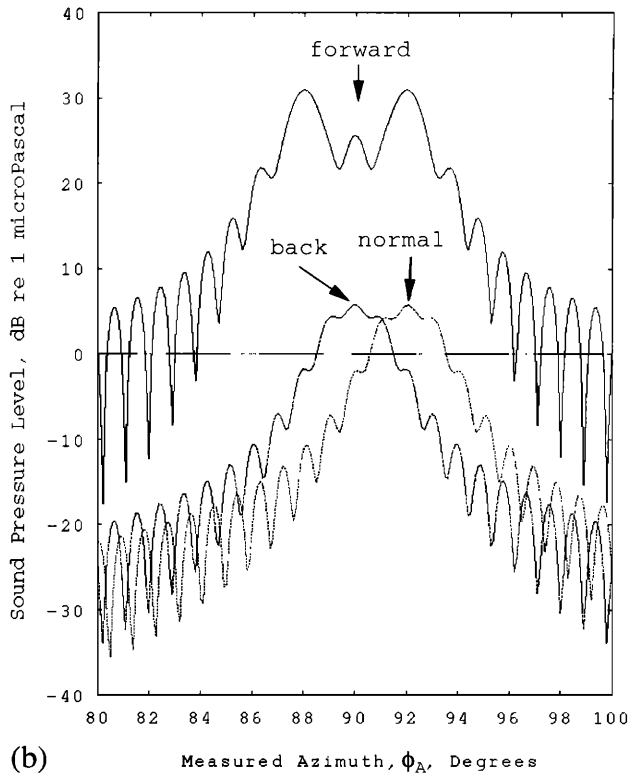

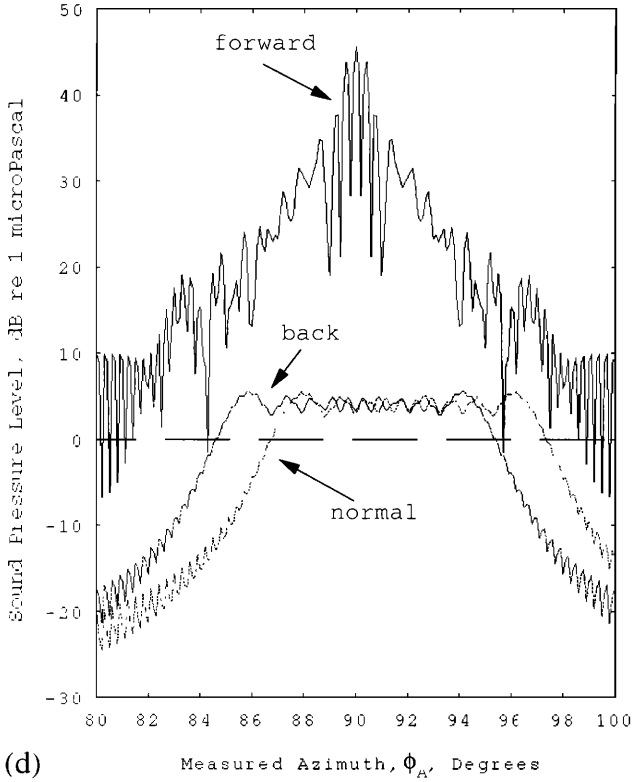

FIG. C5. Simulated measurements for the detection geometry and parameters shown in Fig. C4. In all examples, the scattered field is computed by the exact summation of Eqs. (C1)–(C2): (a) the magnitude of each of the three fields measured on a $N=129$ element array at $\rho=20$ m; (b) the measured directional spectrum of the same array as in (a). The reflected arrivals have width greater than the $\lambda/L=0.9°$ broadside resolution of the array because the measurement is well within the Fraunhofer zone of the array and object. (c) The $N=129$ element array is roughly at the Fraunhofer range of the array and object at $\rho=200$ m. Forward scattering interference is greater than the previous example. The resolution of the array is insufficient to distinguish reflected arrivals, which are truly specular. (d) The array aperture, and number of elements, is increased by a factor of 3 at $\rho=20$ m. The main peaks of the measured reflected spectra show increased width.

Redistribution subject to ASA license or copyright; see http://acousticalsociety.org/content/terms. Download to IP: 18.38.0.166 On: Mon, 12 Jan 2015 18:30:17

Here we have used the far-field asymptote for the Bessel function, and have assumed that $\rho \gg \Delta r$. The expectation values and therefore the cross terms $C_{SN}(\mathbf{r},\mathbf{r}')+C_{NS}(\mathbf{r},\mathbf{r}')$ themselves vanish when $\Delta r \geq \pi/\xi$. Under these circumstances, steep angle propagation will dominate the cross terms. Furthermore, due to higher-order mode stripping, the cross terms will be most significant in close proximity to the scattering object. However, for the relative motion to have any effect at all, even on perfectly horizontal propagation at $\xi=k$, the scale of the fluctuations Δr must be greater than $\lambda/2$. Therefore, this argument is only of significance in the mid to high frequency regime.

We note that by similar arguments it can be shown that $\langle C_{SS}(\mathbf{r},\mathbf{r}')\rangle_{\Delta r}$ does not vanish and is relatively invariant to small random object motions regardless of range and propagation angle. This is due to the presence of squared factors such as $\langle \cos^2[\Delta r(\xi-\xi')]\rangle_{\Delta r}$ and $\langle \sin^2[\Delta r(\xi-\xi')]\rangle_{\Delta r}$ in the scattered field covariance.

The covariance cross terms may also be severely diminished by temporal decorrelation of the source signal over the travel time difference between source–object–receiver and source–receiver paths. In general, the direct and scattered noise fields will be independent if the acoustic travel time between scatterer and receiver is greater than the temporal correlation scale of the noise source. Since a typical correlation time scale for a surface noise source is on the order of $\tau=1$ s,[20] we deduce that covariance cross terms will not be negligible for detections within roughly $c\tau/2=750$ m of the object. Also, the contribution to covariance cross terms will not be negligible from sources where the path length difference in source–object–receiver versus source–receiver paths is less than $c\tau/2$. This condition selects sources in a sector extending behind the object from the sensor which is symmetric about the line joining the two.

[1] S. Flatté and W. Munk, "Submarine detection: Acoustic contrast versus acoustic glow," JASON Report JSR-85-108 (MITRE Corp., McLean, Virginia, 1985).

[2] K. Case, R. Davis, S. Flatté, and F. Zachariasen, "Occultation Study Summary," JASON Report JSR-86-108 (MITRE Corp., McLean, Virginia, 1987).

[3] M. J. Buckingham, B. V. Berkhout, and S. A. L. Glegg, "Imaging the ocean with ambient noise," Nature **356**, 327–329 (1992).

[4] M. J. Buckingham, "Theory of acoustic imaging in the ocean with ambient noise," J. Comp. Acoust. **1**, 117–140 (1993).

[5] F. Ingenito, "Scattering from an object in a stratified medium," J. Acoust. Soc. Am. **82**, 2051–2059 (1987).

[6] W. A. Kuperman and F. Ingenito, "Spatial correlation of surface noise in a stratified ocean," J. Acoust. Soc. Am. **67**, 1988–1996 (1980).

[7] N. C. Makris, W. A. Kuperman, and F. Ingenito, "Detection of a submerged object insonified by surface noise in an ocean waveguide," J. Acoust. Soc. Am. **92**, 2416(A) (1992).

[8] N. C. Makris, W. A. Kuperman, and F. Ingenito, "Bounds on the detection of a submerged object insonified by surface noise in a shallow water waveguide," in *Sea Surface Sound '94*, edited by M. J. Buckingham and J. R. Potter (Kluwer Academic, Dordrecht, 1994).

[9] J. J. Bowman, T. B. A. Senior, and P. L. E. Uslenghi (Eds.) *Electromagnetic and Acoustic Scattering by Simple Shapes* (North-Holland, Amsterdam, 1969).

[10] W. M. Carey, R. B. Evans, J. A. Davis, and G. Botseas, "Deep-ocean vertical noise directionality," IEEE J. Oceanic Eng. **15**, (4), 324 (1990).

[11] Personal communication with W. M. Carey.

[12] D. J. Kewley, D. G. Browning, and W. M. Carey, "Low-frequency wind-generated ambient noise source levels," J. Acoust. Soc. Am. **88**, 1894–1902 (1990).

[13] D. H. Johnson, "The application of spectral estimation methods to bearing estimation problems," Proc. IEEE **70**, 1018–1028 (1982).

[14] A. B. Baggeroer, W. A. Kuperman, and H. Schmidt, "Matched field processing: Source localization in correlated noise as an optimum parameter estimation problem," J. Acoust. Soc. Am. **83**, 571–587 (1988).

[15] Au (Ed.), *The Sonar of Dolphins* (Springer-Verlag, New York, 1993).

[16] H. L. Van Trees, *Detection, Estimation and Modulation Theory, Part III* (Wiley, New York, 1970).

[17] M. D. Collins, N. C. Makris, and L. T Fialkowski, "Noise cancellation and source localization," J. Acoust. Soc. Am. **96**, 1773–1776 (1994).

[18] J. R. Potter, "Acoustic Imaging using ambient noise: Some theory and simulation results," J. Acoust. Soc. Am. **95**, 21–33 (1994).

[19] M. Born and E. Wolf, *Principles of Optics* (Pergamon, New York, 1980).

[20] P. H. Dahl, "High Frequency Noise Emitted from Ocean Breaking Waves," in *Sea Surface Sound '94*, edited by M. J. Buckingham and J. R. Potter (Kluwer Academic, Dordrecht, 1994).

Redistribution subject to ASA license or copyright; see http://acousticalsociety.org/content/terms. Download to IP: 18.38.0.166 On: Mon, 12 Jan 2015 18:30:17